

Modeling Heatshield Erosion due to Dust Particle Impacts for Martian Entries

Grant Palmer¹

AMA, Inc. at NASA Ames Research Center, Moffett Field, CA, 94035, United States

Eric Ching² and Matthias Ihme³

Stanford University, Stanford, CA, 94305, United States

Dirk Kerkhoff⁴ and Ali Gülhan⁵

German Aerospace Center (DLR), Cologne, Germany

Heatshield design for spacecraft entering the atmosphere of Mars may be affected by the presence of atmospheric dust. Particle impacts with sufficient kinetic energy can cause spallation damage to the heatshield that must be estimated. The dust environment in terms of particle size distribution and number density can be inferred from ground-based or atmospheric observations at Mars. Using a Lagrangian approach, the particle trajectories through the shock layer can be computed using a set of coupled ordinary differential equations. The dust particles are small enough that non-continuum effects must be accounted for when computing the drag coefficient and heat transfer to the particle surface. Surface damage correlations for impact crater diameter and penetration depth are presented for fused-silica, AVCOAT, Shuttle tiles, cork, and Norcoat Liège. The cork and Norcoat Liège correlations are new and were developed in this study. The modeling equations presented in this paper are applied to compute the heatshield erosion due to dust particle impacts on the ExoMars Schiaparelli entry capsule during dust storm conditions.

I. Nomenclature

A	=	area, m ²
c_p	=	specific heat at constant pressure, J/kg-K
C_d	=	drag coefficient
C_h	=	heat transfer coefficient, W/m ² -K
$d_z \tau$	=	dust opacity, 1/km
D_c	=	impact crater diameter, m
e_{int}	=	internal energy, J/kg
h	=	enthalpy, J/kg
Kn	=	Knudsen number
L_s	=	solar longitude, deg
m	=	mass, kg
M	=	Mach number
Nu	=	Nusselt number

¹ Research Scientist, Aerothermodynamics Branch, AIAA Associate Fellow.

² PhD Student, Department of Mechanical Engineering, Stanford University, AIAA Member.

³ Professor, Institute for Computational and Mathematical Engineering, Stanford University.

⁴ Research Scientist, German Aerospace Center (DLR).

⁵ Department head, Institute of Aerodynamics and Flow Technology.

N_v	= volumetric number density, $1/m^3$
p	= pressure, N/m^2 or impact crater penetration depth, m
Pr	= Prandtl number
q	= mass mixing ratio
\dot{q}	= rate at which energy changes inside particle, W/m^3
q_{conv}	= convective heating rate, W/m^2
Q_{ext}	= extinction coefficient
r	= radius, m
R	= Universal gas constant, 8.314462 J/kg-mole
Re	= Reynolds number
t	= time, s
T	= temperature, K
V	= velocity, m/s
κ	= thermal conductivity, W/m-K
μ	= viscosity, kg/m-s
ρ	= density, kg/m^3
ζ	= latent heat of vaporization, J/kg
τ	= column optical depth or total column opacity

Subscripts

g	= gas
m	= mode
p	= particle

II. Introduction

One of the unique aspects of designing a spacecraft that will enter the Martian atmosphere is that the vehicle will encounter dust during atmospheric entry. Small dust particles are present even under quiescent conditions, and the level of dust significantly increases when a major dust storm occurs. During or after a dust storm, the dust can extend to altitudes as high as 80 km [1]. Based on measurements taken by the Viking landers and estimations of the strength of the vertical winds in the Martian atmosphere, it was determined that the residence time of the larger (5–10 μm diameter) particles in the upper atmosphere was between 20 and 50 days after the beginning of a major dust storm [1].

Observations and analysis of atmospheric conditions during Martian dust storms have taken place since the Mariner 9 spacecraft obtained infrared spectra data during the 1971-72 dust storm [2]. Measurements, both land-based and from spacecraft orbiting the planet, have continued to obtain data on Martian atmospheric dust whenever possible since the 1970s. Based on observations taken over decades, major global dust storms occur on the average of once every 3–4 Earth years. They do not, however, happen at regular intervals. For example, two major global dust storms occurred in 1977. In the 21st century, major global dust storms have occurred in 2001, 2007, and 2018. Photos of Mars before and during the 2018 global dust storm are shown in Fig. 1.

Because planetary missions to Mars take years from initial design to arrival at Mars, and because of the unpredictability of major global dust storms, the design of the thermal protection system (TPS) of a Mars entry vehicle requires an estimation for the potential damage caused by dust particle impacts on the heatshield. Dust particle erosion can increase the required TPS thickness and/or increase risk due to leaner margins.

An early attempt to estimate heatshield erosion due to dust particle impacts was performed by Papadopoulos, et al. [3], who used a computational fluid dynamic (CFD) flow solver in conjunction with a Lagrangian particle trajectory code to compute heatshield erosion on a 26-meter diameter, 70-deg sphere-cone entry vehicle. Palmer, et al. [4] used the same technique as Ref. [3] but with an updated atmospheric dust model applied to the Mars 2001 Lander entry vehicle. The fluid dynamic and particle trajectory simulations in Refs. [3] and [4] were computed separately under the assumptions that the dust particles were small and disperse enough such that the particles did not affect the shock layer flow. Papadopoulos, et al. recognized that Martian dust particles are small enough that they will be in a non-continuum flow regime when they travel through the shock layer, and non-continuum effects must be accounted for when evaluating the drag coefficient and heat transfer to the particle.

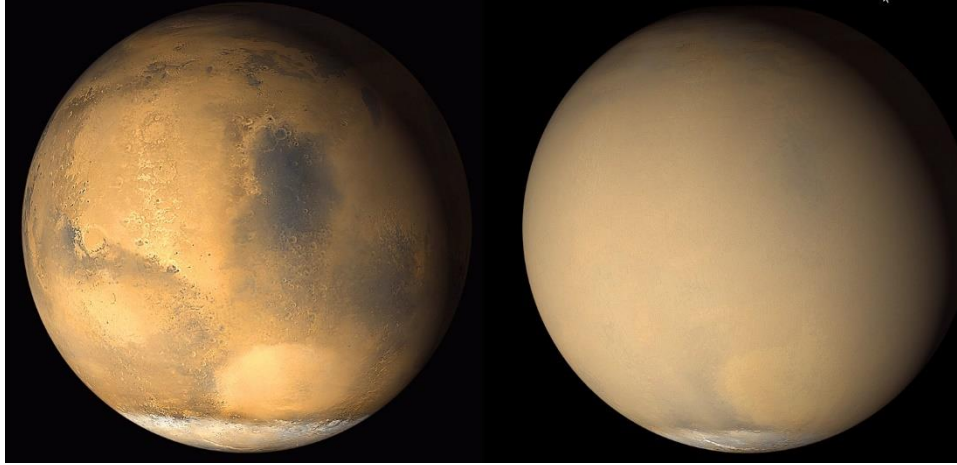


Fig. 1 Photos taken before (left) and during (right) the 2018 global Martian dust storm.

Other researchers have integrated the particle and fluid dynamic equations in a two-way coupling scheme where the particles and shock layer flow impact each other. Elangovan and Cao [5] performed a 2-D analysis using an Eulerian approach for both the particles and fluid dynamics where the particle trajectory and fluid dynamic equations were solved together using the same CFD grid. Saito, et al. [6] used a similar 2-D Eulerian approach to simulate dusty flow around a wedge geometry. Marois, et al. [7] used an Eulerian approach for both the particles and fluid dynamics. Ching, et al. [8] developed a Lagrangian particle tracking methodology using a high-order discontinuous Galerkin (DG) scheme. This approach was applied to compute coupled particle-fluid simulations of high-speed dusty flows over blunt bodies [9]. References [5] through [9] did not include estimates of heatshield erosion due to dust particle impacts, but instead focused on simulating effects such as surface heating augmentation and shock layer disturbances caused by the presence of dust particles.

This paper will provide an overview of the equations and modeling assumptions that go into an analysis of heatshield erosion due to dust particle impacts during a Martian entry. The intent is to summarize and synthesize previous work to provide a single reference that provides all necessary information to perform an analysis of augmented heatshield erosion due to the presence of dust particles. Some of the original references on surface damage models or particle dynamics are difficult to find. Many of the older references use a mixed system of units in the equations they present (e.g. gm/cm^3 for density, km/s for velocity, mm for impact crater depth, etc.), and in some cases equations are presented without explaining what the units are. Some of the early, landmark papers on particle flow analysis contain errors in the equations they present that are not apparent without going through the full derivation.

The equations for determining the size distribution and number density of dust particles as a function of altitude based on observations taken at Mars are discussed. The particle trajectory equations using the Lagrangian framework are presented. Surface damage correlations are presented for five TPS materials as a function of particle density, diameter, and impact velocity including new surface damage correlations for cork and Norcoat Lège. The dust environment, particle trajectory, and surface damage models presented in this paper are applied to estimate the heatshield erosion due to dust particle impacts for a hypothetical case of the ExoMars Schiaparelli capsule entering the Martian atmosphere during a major regional and global dust storm.

III. Martian Dust Environment

In order to estimate the heatshield erosion due to dust particle impacts, the dust environment encountered by the spacecraft during its entry into the Martian atmosphere must be modeled. Dust particles are always present in the Martian atmosphere to some extent. Weather systems range from localized dust devils up to a few hundred meters in height [10] to major global dust storms that can inject additional quantities of dust vertically into the atmosphere as high as 50-80 km above the surface where it can be transported over long distances by the Martian wind systems. The amount of dust in the atmosphere depends on the time of year, whether there is a local, regional, or global dust storm occurring, and location on the planet. Dust levels also tend to increase during the daytime as compared to nighttime [11].

A. Dust Particle Size Distribution

Dust particles lifted from the surface of Mars into the atmosphere are not of uniform size, and to analyze dust particle impacts, the size and number density of the dust particles must be characterized and modeled. A commonly used mathematical equation to represent the atmospheric particle size distribution is the four-parameter modified gamma distribution function (MGD) [12] for a given particle radius, r_p .

$$N(r_p) = N_0 r_p^\mu \exp\left(-(\mu/\gamma)\left(r_p/r_m\right)^\gamma\right) \quad (1)$$

The μ and γ terms in Eq. (1) define the shape of the distribution, and the N_0 term controls the overall scaling. The four-parameter MGD is commonly used to describe the distribution of Martian dust particle sizes, e.g. [13] and Refs. [2] – [4]. Based on analysis of the Mariner 9 spectrometer data taken during the 1971 dust storm, Toon, et al. [2] suggest values of $\mu = 2$ and $\gamma = 1$ such that:

$$N(r_p) = N_0 r_p^2 \exp\left(-4\left(r_p/r_m\right)^{0.5}\right) \quad (2)$$

The modal value of the particle radius, r_m , defines the shape and peak value of the particle distribution. Decreasing the mode radius value compresses the curve to the left, increasing the number of smaller radius particles. Earlier studies such as Toon, et al. [2] and Papadopoulos, et al. [3] used a value of 0.4 micron for the mode radius. Tomasko, et al. suggest a value of 0.32 micron [14]. However, more recent observations by the Mars Climate Sounder (MCS) [13] and computations using the NASA Ames General Circulation Model (GCM) [15] can be used to estimate a more precise value of mode radius based on atmospheric conditions on Mars. The modified gamma distribution based on mode radii of 0.32, 0.35, and 0.40 microns is shown in Fig. 2.

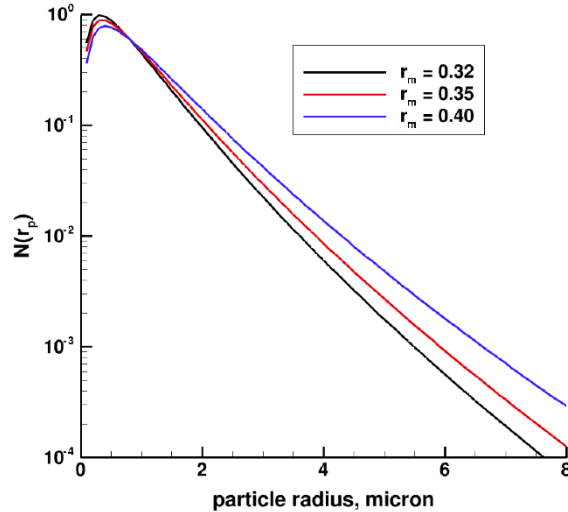


Fig. 2 Modified gamma distribution function based on different mode radius values.

To obtain the fractional amount of a specified particle radius in the distribution (i.e. the volumetric number fraction), $N_f(r_p)$, the gamma distribution value for that radius is divided by the integral of the gamma distribution over all particle radii considered.

$$N_f(r_p) = \frac{N(r_p)dr_p}{\int N(r_p)dr_p} \quad (3)$$

The formal definition of the term, $N(r_p)dr_p$, is that it represents the number of dust particles per unit volume with radii between r_p and $r_p + dr_p$. Most previous studies on heatshield erosion due to dust particle impacts assume that the particles are spherical and of constant composition throughout the particle. These assumptions allow the mass of an individual particle to be related to the particle radius.

$$m_p = \rho_p \frac{4}{3} \pi r_p^3 \quad (4)$$

Assuming that the composition of particles of different radii is the same, the mass fraction of a given particle radius, $N_m(r_p)$, a value required for the damage assessment, is found by multiplying the gamma distribution for a given radius by the spherical volume for that radius divided by the integral of those two quantities over the entire distribution.

$$N_m(r_p) = \frac{r_p^3 N(r_p) dr_p}{\int r_p^3 N(r_p) dr_p} \quad (5)$$

The number and mass fractions for the modified gamma distribution with a mode radius of 0.35 micron is shown in Fig. 3. In terms of number fraction, the most prevalent particle radius is equal to the mode radius value of 0.35 micron. The mass fractions are more weighted to the larger radius values, and the radius with the largest mass fraction is 2.2 micron.

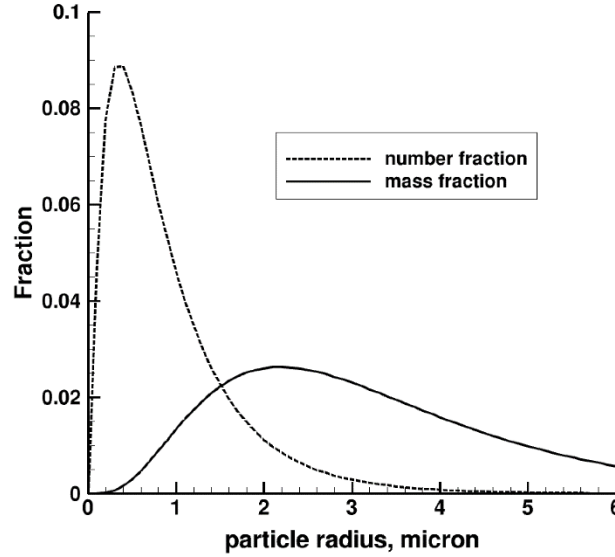


Fig. 3 Number and mass fraction as a function of particle radius, $r_m = 0.35$ micron.

Since it is impractical to consider every possible particle radius in a particle damage assessment, the full MGD can be “binned” into discrete particle radii values. Figure 4 shows the MGD for a mode radius of 0.35 micron binned into 15 discrete particle radii values ranging from 0.5 to 9 microns. The largest mass fractions in the binned distribution are for particle radii of 2.0 and 2.5 micron.

B. Effective Particle Radius

An important parameter in describing the dust environment, particularly for incorporating experimental observations at Mars into mathematical correlations, is the effective particle radius, r_{eff} , which is defined as the integral of the cube distribution of the dust particle radius divided by the integral of the square of the particle radius over the distribution.

$$r_{eff} = \frac{\int_0^{\infty} r_p^3 N(r_p) dr_p}{\int_0^{\infty} r_p^2 N(r_p) dr_p} \quad (3)$$

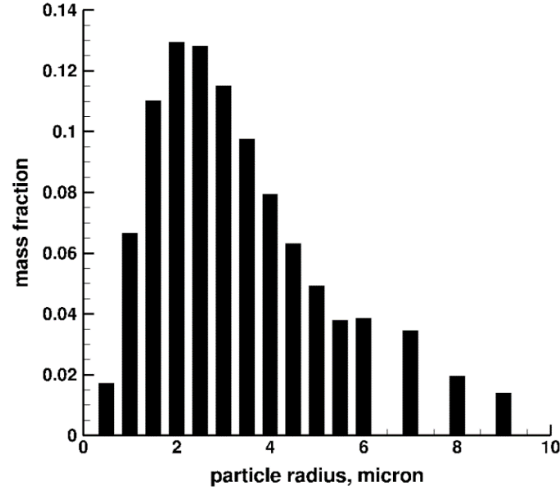


Fig. 4 Binned particle mass fractions, $r_m = 0.35$ micron.

The effective particle radius is not the average particle radius over the distribution but rather is proportional to the ratio of the average particle volume divided by the average particle surface area. Values for the effective particle radius can be estimated based on observations taken in the Martian atmosphere or from detailed numerical simulations. For example, Chen-Chen, et al. [16] estimated effective particle radius and dust optical depth at the Gale Crater on Mars by analyzing observations of sky brightness as a function of scattering angle from the navigation cameras of the Mars Science Laboratory (MSL) rover Curiosity. Based on observations taken over more than two Martian years, the effective particle radius varied from 0.86 – 2.02 microns. Using data from the Thermal Emission Spectrometer (TES) aboard the Mars Global Surveyor (MGS), Wolff and Clancy [17] estimated effective particle radius values for moderate to low dust loading conditions to range between 1.4 and 1.6 micron.

Effective radius values increase during dust storms. Using spectral data taken from the MGS, Kahre, et al. [15] used the NASA Ames General Circulation Model (GCM) to estimate spatial and temporal variations in Martian dust particle sizes. Their results for a simulated global dust storm showed effective particle radii ranging from 1.6 – 2.5 microns. Wolf and Clancy [17] used data from the MGS TES to estimate effective radius values ranging from 1.3 to 3.0 microns (depending on latitude) that occurred near the peak of the 2001 global dust storm.

The effective radius can be used to calibrate the value of the mode radius used in the modified gamma distribution. If the effective radius value is known from observations on Mars or detailed computer simulations, the mode radius of the MGD can be adjusted until the effective radius calculated by the modified gamma distribution matches the desired value. Table 1 lists the effective radius computed using the MGD shown in Eq. (2) as a function of mode radius

Table 1. Effective radius as a function of mode radius

r_m , micron	r_{eff} , micron
0.15	1.031
0.20	1.375
0.25	1.717
0.30	2.056
0.35	2.387
0.40	2.706
0.45	3.010

C. Total Particle Number Density and Mass Mixing Ratio

Along with the distribution of particle sizes, the total particle volumetric number density must also be determined. There is a strong correlation between volumetric number density (i.e. the number of particles per unit volume), N_v , of dust particles and the dust opacity, $d_z\tau$, which represents the fractional extinction per unit height of radiative emission due to dust [13].

$$d_z\tau = N_v Q_{ext} \int_0^\infty \pi r_p^2 N(r_p) dr_p = N_v Q_{ext} G \quad (4)$$

The quantity, G , in Eq. (4) is the average geometric cross section of the particle distribution assuming a circular cross section shape. Another important quantity to assess is the mass mixing ratio, q , (also referred to as the mass loading ratio) that is defined as the ratio of the mass of dust in the atmosphere per unit volume divided by the mass of atmospheric gas per unit volume.

$$q = \frac{\rho_p N_v}{\rho} \int_0^\infty \frac{4}{3} \pi r^3 N(r_p) dr_p \quad (5)$$

The integral quantity in Eq. (5) is the average particle volume over the distribution assuming a spherical particle shape. Using Eqs. (3) and (4), the mass mixing ratio can be expressed in terms of the dust opacity and effective particle radius.

$$q = \frac{4}{3} \frac{\rho_p}{Q_{ext}} \frac{d_z\tau}{\rho} r_{eff} \quad (6)$$

The quantity, $d_z\tau/\rho$, is known as the density-scaled opacity and has units of m^2/kg , as compared to opacity which is typically expressed in units of km^{-1} . Based on Eq. (6), if the density-scaled opacity is increased, the mass mixing ratio will increase by a proportional amount.

The value of the extinction coefficient, Q_{ext} , is dependent on the particle size distribution [13]. Table 2 shows values for the ratio, Q_{ext}/r_{eff} , taken from Ref. [13] that are based on Mie scattering simulations of MCS data. Once the effective radius is known, whether from observations on Mars or by evaluating the MGD equation, the value of the extinction coefficient can be obtained.

Table 2. Ratio of extinction coefficient to effective radius from Ref. [13].

r_{eff} , micron	Q_{ext}/r_{eff}
0.75	0.3095
1.06	0.3305
1.50	0.3619
2.12	0.3956
3.00	0.4137
4.24	0.3998

The vertical distribution of dust opacity in the Martian atmosphere can be evaluated from measurements taken by the MCS onboard the Mars Reconnaissance Orbiter (MRO) [18]. The MCS has been making global, moderate vertical resolution observations of infrared radiance in nine broadband channels sensitive to dust, temperature, and other aerosols since 2006. Atmospheric retrievals from MCS observations include vertical profiles of temperature and dust opacity at 463 cm^{-1} [13]. The MCS retrieval algorithm is based on the dust being compositionally uniform and made of spherically symmetric particles.

D. Vertical Distribution of Dust Particles

Considering the effects of sedimentation and mixing during a global dust storm, Conrath [19] derived an equation for the mass mixing ratio that accounts for the fact that dust levels tend to decrease with increasing altitude. Originally expressed in terms of a scale height, Forget, et al. [20] redefined the Conrath equation in terms of a pressure ratio between the surface pressure, p_0 , and the pressure at the desired altitude, p .

$$q = q_0 \exp \left[v \left(1 - (p_0/p)^{z_0/z_{max}} \right) \right] \quad (7)$$

The surface pressure at Mars is approximately 700 N/m². The parameter q_0 is the mass mixing ratio at the surface. The Conrath parameter, v , represents the ratio between the characteristic dust diffusion time and characteristic dust sedimentation time at the surface. Kahre, et al. [15] suggested that a Conrath parameter of 0.05 provided the best fit to their simulation using the NASA Ames General Circulation Model. However, Forget, et al. [20] recommended a value of 0.007 as a fit to the Mariner 9 data of the 1971 dust storm. Decreasing the value of the Conrath parameter increases the mass mixing ratio at higher altitudes. The parameter z_{max} is the maximum height of observed dust, and Z_0 is a reference height. Chen-Chen, et al. [16] suggest a value of 70 km for Z_0 , but the appropriate value may be a function of z_{max} .

As previously stated, during major global dust storms increased dust particle levels can be observed as high as 80 km above the surface of Mars. Intuitively, it makes sense to assume that the distribution of dust particles would change with altitude in that it would be easier for the wind currents to lift smaller, lighter dust particles to the upper altitudes compared to the larger, heavier particles. If the effective radius could somehow be estimated as a function of altitude, the mode radius in the modified gamma distribution could similarly be adjusted as a function of altitude. Kahre, et al. [15] state that the largest particle effective radius occurs at the surface and decreases with increasing altitude. They present contour plots in Ref. [15] of effective particle radius as a function of atmospheric pressure (i.e altitude), but don't provide a general correlation for effective particle radius as a function of altitude. Kahre, et al. also state in Ref. [15] that there is no need to invoke a spatially- or temporally-varying lifted dust distribution, i.e. that the same particle size distribution can be used at all (reasonable) altitudes. This assumption was also made by Wolff and Clancy [17]. Toon, et al. [2] state that based on examination of pictures taken by the Mariner 9 spacecraft the dust size distribution did not change significantly during the decay of the 1971 dust storm. Due to the ambiguity on this subject in the existing literature, a constant value of effective particle radius will be assumed for the analysis presented in this study.

E. Dust Particle Shape and Composition

Toon, et al. [2] deduced from the Mariner 9 data that the dust particle shapes were plate-like, but most researchers (e.g. Refs. [2] – [4]) assume that the particles are spherical and of uniform composition, and these assumptions are used in the present study. Assuming a spherical shape with constant composition allows a direct correlation between particle mass and radius and simplifies the estimation of particle drag coefficient and surface heat transfer.

Estimates of dust particle density in the literature range from 2400 – 3000 kg/m³ and depend on the assumed elemental composition of the particles. Toon, et al. [2] presented a detailed analysis of dust particle composition based on observations taken by the Mariner 9 spacecraft during the 1971-72 dust storm. They deduced that the dust particles were 50-70% SiO₂ with the remainder being various oxides. Pure SiO₂ has a density of 2650 kg/m³. Papadopoulos, et al. [3] assumed a Martian dust particle composition of 70% SiO₂, 15-20% Al₂O₃, and the rest being iron oxides and trace compounds with a combined density of 2940 kg/m³. Heavens, et al. [11] used a value of 3000 kg/m³ for their analysis as did Murphy, et al. [21]. In this study, the value of dust particle density recommended in Ref. [3] of 2940 kg/m³ was used.

F. Conditions During Major Regional or Global Dust Storms

There is always some level of dust present in the Martian atmosphere. Localized wind currents such as dust devils can lift dust from the surface to altitudes of several hundred meters [10]. If the conditions are right, these localized dust disturbances can grow into a major regional or global dust storm. A major global dust storm occurred on Mars in 2001, corresponding to Mars Year (MY) 25. It was the largest dust storm observed for several decades. Another global dust storm occurred in 2007 (MY 28). A major regional dust storm covered the Southern hemisphere of Mars in November 2012 (MY 31). A very large global dust storm took place in 2018 (MY 34), and this storm disabled the NASA Opportunity rover.

During a regional or global dust storm, dust levels will be higher and the dust will be transported to higher altitudes compared to non-dust event conditions. MCS data for dust opacity as a function of atmospheric pressure, which can

be converted to altitude, can be obtained from the NASA Planetary Data Systems (PDS) website [22]. The MCS has been in operation since Sept 2006, so MCS data is not available for the 2001 dust storm. As of the publication of this paper, MCS data is only available up to April 2015, so MCS data for the 2018 dust storm is not yet available.

Fortunately, MCS data is available from the PDS website for the 2007 and 2012 dust storms. There is a lot of MCS data, and the profiles of dust opacity as a function of altitude vary depending on the date, time of day, and geographic location on Mars. Profiles were selected from the MCS database that represented more severe conditions during the 2007 and 2012 dust storms. MCS data was also extracted for a profile from October 2012 prior to the onset of the November 2012 dust storm. The MCS data for the selected 2007 profile was only available for altitudes greater than 37.5 km, and the Conrath equation was used to extend the October 2012 MCS profile down to the surface. Similarly, the selected November 2012 MCS data only extended down to 22.8 km. The data for October 2012 went down to an altitude of 8.7 km. From the data cut-off point, the Conrath equation was similarly used to extend the 2012 MCS data down to the surface.

Figure 5 shows density-scaled dust opacity, mass mixing ratio, and particle number density profiles for the selected 2007 and 2012 dust conditions. The density-scaled opacity data (whether from MCS data or extrapolated using the Conrath equation) was used to compute the mass mixing ratio and particle number density. The profiles for the 2007 and November 2012 dust storm conditions were based on an effective radius of 2.2 micron and a Q_{ext}/r_{eff} ratio of 0.4. The October 2012 profiles, taken during quieter dust conditions, were based on an effective radius of 1.5 micron and a corresponding extinction coefficient ratio of 0.3619.

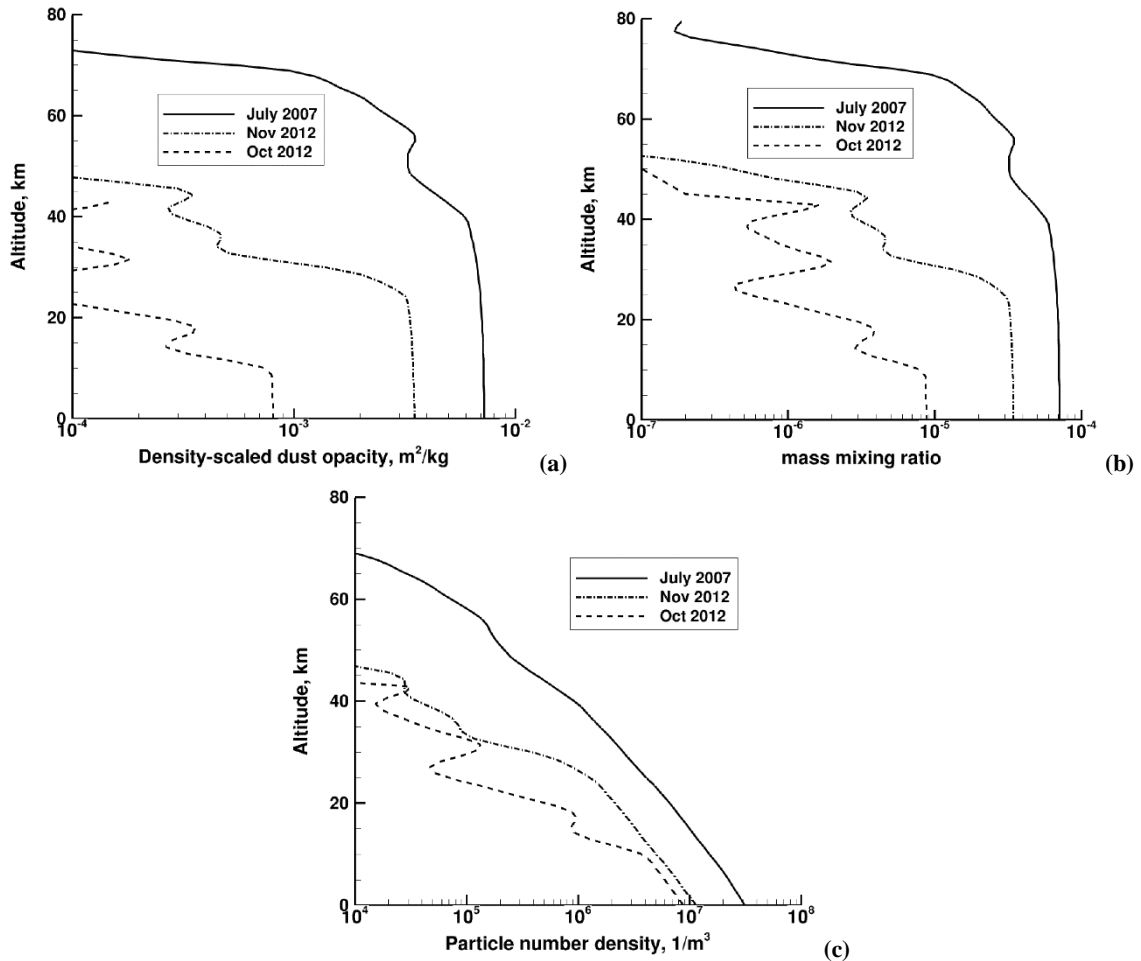


Fig. 5 Dust conditions during and before major dust storms. (a) Density-scaled dust opacity. (b) Mass mixing ratio. (c) Particle number density.

It is not surprising that the existence of a regional or global dust storm causes elevated dust levels compared to the October 2012 profile. Examining the profiles in Fig. 4, the 2007 dust storm was stronger than the 2012 storm. The dust levels in 2007 were higher throughout the altitude profile, and there was measurable dust as high as 80 km. It is also apparent from Fig. 4 that the mass mixing ratio profiles derived from the MCS data don't always follow the smooth exponential curve predicted by the Conrath equation.

Most of the heatshield erosion due to dust particle impacts will occur at altitudes above 20 km. Table 3 lists the density-scaled dust opacity, mass mixing ratio, and particle number density for the three profiles at an altitude of 20 km. The July 2007 particle number density is 12.4 times higher than the pre-dust storm level seen in October 2012. The more moderate November 2012 dust storm saw particle number densities that were 4.0 times higher than the October 2012 values. Keep in mind that the assumed effective particle radius was larger for the 2007 and November 2012 conditions, and the combination of larger average particle size with higher overall particle number density will result in significantly more heatshield erosion. Also, there is significant variability in the MCS data depending on time and geographic location, so the factors of 12.4 and 4.0 are merely representative of how much dust levels increase during major dust storms.

Table 3. Dust environment at 20 km altitude during and before major dust storms.

Date	Dust Event	$d_z \tau / \rho$, m ² /kg	Mass mixing ratio	N_v , 1/m ³
July 2007	Global storm	7.049e-3	6.917e-5	6.621e+6
Oct 2012	None	2.838e-4	2.683e-6	5.331e+5
Nov 2012	Regional storm	3.343e-3	3.276e-5	2.147e+6

IV. Particle Trajectory Analysis

For dust particles to cause surface erosion of the heatshield during a Martian entry, the particles must first travel through the shock layer between the bow shock wave and the vehicle. As the spacecraft travels along its entry trajectory, dust particles will enter the bow shock at approximately the velocity of the spacecraft (dust velocity due to Martian wind currents is neglected). The fluid inside the shock layer will have significantly higher density and temperature than the freestream conditions, so the particles will slow down and heat up as they travel towards the heatshield. The fluid will also bend the particle trajectories to follow the direction of the gas flow. Because they are traveling at different velocities and are at different temperatures, the particles and fluid can exchange momentum and energy.

The degree to which the shock layer flow affects the particles depends on the particle size. Smaller particles will slow down and heat up to a greater extent compared to larger particles. If the particles are large enough, they will be relatively unaffected as they travel through the shock layer and will strike the heatshield at nearly the aeroshell velocity. This effect is shown in Fig. 6 where 1- and 5-micron radius particles travel through a Mach 13 shock layer at an altitude of 30 km. The colors inside the circles indicate particle velocity compared to that of the surrounding fluid. The 1-micron particles slow down significantly as they travel through the shock layer. The flow bends the particle trajectories downward such that 5 of the 6 particles shown don't strike the heatshield. Conversely, the 5-micron particles are less affected by the surrounding fluid. The particles do slow down, but to a lesser extent compared to the 1-micron particles. Similarly, the 5-micron particle trajectories are relatively unaffected by the flow direction, and 5 of the 6 particles shown do strike the heatshield.

One approach to compute particle trajectories is to use a Lagrangian framework where the location and state of individual particles are tracked as the particles move through the shock layer. The particle trajectory equation developed and presented in this section assumes that the particles are spherical and of constant composition, an assumption made by most, if not all, previous authors. The computation of particle trajectories using the Lagrangian framework involves the solution of a series of coupled ordinary differential equations (ODEs).

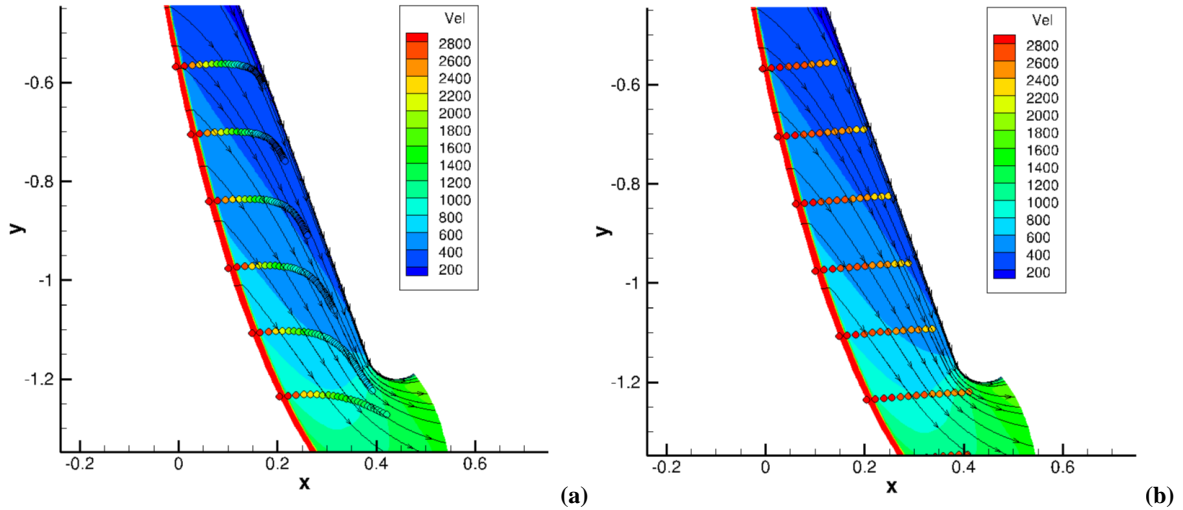


Fig. 6 Particle velocities overlaid on shock layer velocity. (a) 1-micron radius particles. (b) 5-micron radius particles

A. Fluid-Particle coupling

One of the modeling decisions needed to perform an analysis of heatshield erosion due to dust particle impacts is the degree of fluid-particle coupling. There are four general levels of modeling complexity, each one requiring more computational resources while allowing the inclusion of more sophisticated physics relative to the previous level.

1. No Coupling

The simplest approach to particle trajectory analysis is to assume there is no coupling between the particles and the shock layer flow. Under this assumption, the particles are unaffected as they pass through the shock layer and strike the heatshield with the full relative (i.e. aeroshell) velocity. This assumption is only valid if the particles are large and/or the shock layer density is low. Generally speaking, assuming no fluid-particle coupling will over-estimate heatshield erosion.

2. One-Way Coupling

With one-way coupling, the shock layer flow is assumed to affect the particle trajectories, but the particles do not affect the shock layer flow. The shock layer flow and particle trajectories can be computed separately. Typically, the flow solution is computed first by a Navier-Stokes CFD flow solver at multiple points along the entry trajectory. The CFD solutions are then used to compute the particle trajectories through the shock layer as a post-processing step. One-way coupling assumes that the transfer of momentum and energy between the particles and surrounding flow is small. The particles are assumed to be small enough that there is no temperature gradient inside the particle, i.e. the temperature of the entire particle is equal to the surface temperature. The one-way approach is computationally efficient in that the particle trajectories can be computed in seconds. However, one-way coupling cannot model effects such as thermophoretic force, which is caused by a temperature difference between the windward and leeward surfaces of the particle or the augmented surface heating rates that can result from particle impacts and from the presence of particles in the boundary layer. One-way coupling will also ignore the effect of the particles acting as an energy sink in the shock layer.

3. Two-Way Coupling

With two-way coupling, the shock layer flow and particles are assumed to affect each other in that momentum and energy are transferred between the particles and fluid as the particles travel through the shock layer. Because of the transfer mechanisms, the CFD flow solution and particle trajectory computations must be performed at the same time in a coupled manner. The computational resources for two-way coupling is significantly greater than with one-way coupling, but two-way coupling allows the inclusion of effects such as thermophoretic heating. Also, it has been shown experimentally that particle impacts can increase surface heating rates on the vehicle due to energy transfer in the boundary layer, an effect that two-way coupling can model.

4. Four-Way Coupling

Four-way coupling includes collisions between particles in the computational model. Additionally, particles can strike the heatshield and rebound off it at low velocity affecting the shock layer flow. The effect that this phenomenon

has on the ultimate prediction of heatshield erosion rates is not well-understood at this time. Including collisions into the computational model significantly increases the computational cost of the simulation. Four-way coupling will not be covered in detail in this paper.

B. Particle Velocity

The Lagrangian approach to determine the particle velocity as it travels through the shock layer was discussed by Bailey and Hiatt [23] and used by Papadopoulos, et al. [3] in the development of their dust erosion model. It is based on applying Newton's second law of motion where the force acting on the particle is due to the aerodynamic drag on the particle.

$$\vec{F} = m_p \frac{d\vec{v}_p}{dt} = \frac{1}{2} \rho_g \cdot |\Delta \vec{V}| \Delta \vec{V} \cdot C_d A \quad (8)$$

Aerodynamic drag force acts along the velocity vector of the particle. The velocity term on the right-hand side of Eq. (8), $\Delta \vec{V} = \vec{v}_g - \vec{v}_p$, is the relative velocity magnitude between the dust particle and the surrounding fluid. The density, ρ_g , in Eq. (8) is that of the fluid surrounding the particle. If the dust particles are assumed to be spherical, the change in particle velocity with time can be expressed in terms of the dust particle diameter, d_p , and density, ρ_p .

$$\frac{d\vec{v}_p}{dt} = \frac{3}{4} \frac{\rho_g C_d}{\rho_p d_p} \cdot |\Delta \vec{V}| \Delta \vec{V} \quad (9)$$

Papadopoulos, et al. [3] used particle diameter in their formulation, rather than particle radius, and that convention is repeated here. Equation (9) represents the magnitude of the change in velocity in that its value will always be positive. The fluid-particle coupling is evident in Eq. (9) in that the equation includes the flow density and velocity. The drag coefficient is also a function of the fluid viscosity.

The key to updating the particle velocity using Eq. (9) is to accurately determine the drag coefficient, C_d , of the dust particle. Martian dust particles are small enough (typically between 1 and 20 microns) and the Martian atmospheric density low enough that the particles will predominantly be in non-continuum flow regimes as they travel through the shock layer. Typical Knudsen numbers based on particle diameter will be greater than 0.1 at lower altitudes and can exceed 2 at altitudes greater than 50 km. Loth [24] defined a particle Knudsen number as the ratio of the mean free path of the surrounding fluid to the particle diameter, which can be written in terms of the particle Mach and Reynolds numbers.

$$Kn = \sqrt{\frac{\pi \gamma}{2}} \left(\frac{M}{Re} \right) \quad (10)$$

The particle Mach and Reynolds numbers are based on the relative particle velocity, $|\vec{v}_g - \vec{v}_p|$. The Reynolds number is also based on the particle diameter, and the fluid density and viscosity.

$$Re = \frac{\rho_g |\Delta \vec{V}| d_p}{\mu_g} \quad (11)$$

The particle Reynolds number value will vary according to the particle size and the surrounding flow conditions but will typically be on the order of 1. Particle Mach numbers will typically be in the subsonic to low supersonic range. The parameter, γ , in Eq. (10) is the ratio of specific heats. The four flow regimes in terms of the particle Knudsen number are shown in Table 4. Martian dust particles will typically experience particle Knudsen numbers in the 0.1 – 2 range as they travel through the shock layer, so they will likely be in the transitional flow regime.

Table 4. Dust particle flow regimes as a function of particle Knudsen number.

Flow Regime	Kn
Continuum	< 0.01
Slip	$0.01 - 0.1$
Transitional	$0.1 - 10$
Free-molecular	> 10

Henderson [25] developed a series of correlations for the drag coefficient of spheres that are applicable for continuum, transitional, and free-molecular flow regimes. The Henderson equations are intended to be consistent with experimental data on spheres taken by Bailey and Hiatt [23] as well as theoretical derivations that date to the early 20th century. It should be noted that the smallest sphere tested in Ref. [23] was 2.38 mm in diameter, which is 2-3 orders of magnitude larger than Martian dust particles. The Henderson correlations are divided into three Mach number regimes.

For subsonic Mach numbers:

$$C_D = 24 \left[Re + S \left\{ 4.33 + \left(\frac{3.65 - 1.53 \frac{T_p}{T_g}}{1 + 0.353 \frac{T_p}{T_g}} \right) \exp \left(-0.247 \frac{Re}{S} \right) \right\} \right]^{-1} + \exp \left(-0.5 \frac{M}{\sqrt{Re}} \right) \left[\frac{4.5 + 0.38(0.03Re + 0.48\sqrt{Re})}{1 + 0.03Re + 0.48\sqrt{Re}} + 0.1M^2 + 0.2M^8 \right] + 0.6S \left[1 - \exp \left(-\frac{M}{Re} \right) \right] \quad (12)$$

The molecular speed ratio, S , in Eq. (12) is a function of particle Mach number, M , and is defined as:

$$S = M \sqrt{\frac{\gamma}{2}} \quad (13)$$

The approach used in Ref. [3] for evaluating the ratio of specific heats, γ , is to use the ratio of static enthalpy to internal energy, β .

$$\gamma = \beta = \frac{h_{st}}{e_{int}} = \frac{h_{st}}{h_{st} - \frac{p}{\rho}} \quad (14)$$

Ching, et al. [8] define the ratio of specific heats using the real-gas value of specific heat at constant pressure and the Universal Gas Constant divided by the gas mixture molar mass.

$$\gamma = \frac{c_p}{c_p - \frac{R}{M}} \quad (15)$$

The value of γ has only a small effect on the particle trajectory for larger particles, but can significantly affect the trajectory of particles with diameters of 1 micron or less.

The subsonic Henderson equation is a rather complicated function of particle Reynolds number, Mach number, and temperature, but it is designed to bridge the various flow regimes. At low Knudsen number, high Reynolds number conditions (i.e. continuum flow), the equation reduces to the Stokes-Oseen equation, $C_d = 24Re^{-1} + 4.5$. If the particle Reynolds number approaches zero, Eq. (12) simplifies to theoretical expressions for free molecular flow. The exponential factors in the second and third terms of Eq. (12) were derived to agree with the experimental data from Ref. [8].

For Mach numbers greater than 1.75, the Henderson model uses the following expression:

$$C_D = \frac{0.9 + \frac{0.34}{M^2} + 1.86 \sqrt{\frac{M}{Re}} \left[2 + \frac{2}{S^2} + \frac{1.058}{S} \sqrt{\frac{T_p}{T_g} - \frac{1}{S^4}} \right]}{1 + 1.86 \sqrt{\frac{M}{Re}}} \quad (16)$$

The supersonic equation is also designed to cover the various flow regimes. For free molecular flow where the Reynolds number approaches zero, the equation reduces to the terms inside the square brackets. For low Knudsen number, high Reynolds number continuum flow, the equation simplifies to the first two terms in the numerator. For supersonic slip and transitional flow, the equation is designed to give good agreement with experimental data in those flow regimes [25].

For particle Mach numbers between 1.0 and 1.75, Henderson recommended a linear interpolation between the drag coefficients at Mach 1 and 1.75.

$$C_D = C_D(1.0) + \frac{4}{3}(M - 1)[C_D(1.75) - C_D(1.0)] \quad (17)$$

A plot of the drag coefficient predicted by the Henderson and Stokes-Oseen models as a function of particle Mach number is shown in Fig. 7a. The particle Reynolds number was held constant at a value of 1, the particle surface temperature was 2800 K, and the surrounding fluid temperature was assumed to be 6025 K. The Henderson curve transitions from the subsonic to supersonic correlation between Mach numbers 1 and 1.75. During a typical Martian entry, particle Mach numbers in the shock layer will range from 2 to 4 with corresponding drag coefficients ranging from 2.8 – 3.2. The particle drag coefficient as function of Reynolds number at a constant particle Mach number of 2 is shown in Fig. 7b. The Stokes-Oseen drag coefficient value for continuum flow will never be lower than 4.5 meaning that it will always be higher than a drag coefficient that accounts for non-continuum effects.

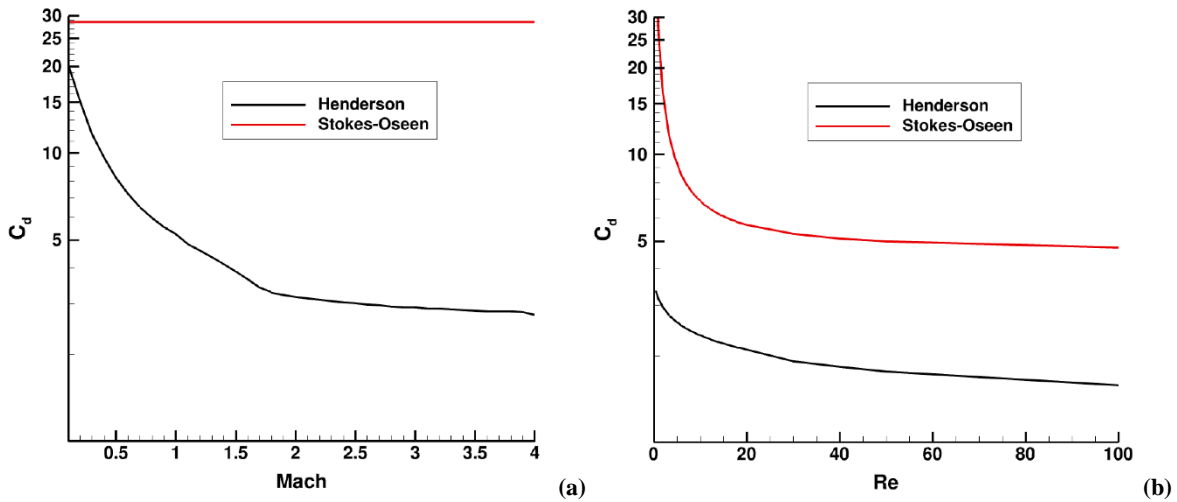


Fig. 7 Dust particle drag coefficient. (a) as a function of Mach number, $Re_p = 1$. (b) as a function of Reynolds number, Mach = 2.

There are other drag models that might be applied to spherical Martian dust particles. Loth [24] presented a series of correlations based on experimental data, theoretical limits and Direct Simulation Monte Carlo (DSMC) simulations. The Loth correlations are complicated, relying on evaluating elements based on the error function for example, and would be cumbersome to implement into a particle trajectory code. Ching and Ihme [26] showed that for particle Mach numbers ranging from 0.3 to 2.0 and particle Reynolds numbers on the order of 1 (the expected conditions for Mars dusty flow analysis) that the Loth and Henderson models give similar values for drag coefficient, within the uncertainty of the experimental data on which the two correlations are based. Boiko, et al. [27] present a drag correlation based on a cloud of particles traveling down a shock tube, but the particle diameters and flow conditions indicate that the particles were in continuum flow, and the correlation from Ref. [27] gives similar results to the Stokes-Oseen equation.

C. Particle Surface Temperature

The fluid in the shock layer will generally be at a higher temperature compared to the freestream. When a dust particle travels through the shock layer, energy will be transferred from the fluid to the particle increasing the particle surface temperature. In the boundary layer, it is possible for the particle temperature to be higher in which case energy would be transferred from the particle back into the fluid. In this paper, it is assumed that there is no temperature

gradient through the particle, i.e. that the temperature of the interior of the particle is equal to the surface temperature. Computing the particle surface temperature is important to assess the heat transfer between the fluid and particle (and vice-versa), because particle temperature affects the drag coefficient, and to account for possible melting or vaporization of the particle.

To assess energy transfer from the fluid to the particle using the Lagrangian framework, the time rate of change of the energy of the particle per unit volume, \dot{q} , is set equal to the rate of energy transfer from the surrounding fluid [28].

$$\dot{q} = \rho_p c_p \frac{dT_p}{dt} \quad (18)$$

Both sides of Eq. (18) have units of W/m³. Neglecting radiative heating, the rate of change of energy of the particle per unit volume is equal to the convective heating rate at the surface, q_{conv} , multiplied by the surface area and divided by the particle volume. If the particles are assumed to be spherical, the change in particle surface temperature can be expressed in terms of the convective heating rate and dust particle diameter

$$\dot{q} = \frac{A_s q_{conv}}{V} = \frac{6q_{conv}}{d_p} = \rho_p c_p \frac{dT_p}{dt} \quad (19)$$

The convective heating rate can be expressed as a function of a heat transfer coefficient, C_h , multiplied by the difference between the temperature at fluid boundary layer edge and the particle surface.

$$q_{conv} = C_h (T_g - T_p) \quad (20)$$

Using Eq. (20), the equation for the change in particle surface temperature as a function of time can be expressed in the form presented in Ref. [3].

$$\frac{dT_p}{dt} = \frac{6C_h}{\rho_p c_p d_p} (T_g - T_p) \quad (21)$$

In order to evaluate Eq. (21), the value of the heat transfer coefficient must be determined. The heat transfer coefficient can be related to the Nusselt number, Nu , which represents the ratio of convective to conductive heat transfer across a boundary.

$$Nu = \frac{C_h L}{\kappa_g} = \frac{C_h d_p}{\kappa_g} \quad (22)$$

For particle trajectory analysis, the characteristic length, L , in the Nusselt number definition is set equal to the particle diameter. The coefficient of thermal conductivity, κ_g , in Eq. (22) is that of the fluid surrounding the dust particle. Since Nusselt number correlations are usually expressed in terms of the particle Mach and Reynolds number, they are therefore functions of the fluid velocity and viscosity as well as the fluid thermal conductivity.

There have been a number of correlations for Nusselt number developed over the years. For continuum flow, Drake [29] derived a correlation based on the Prandtl number of the fluid and the particle Reynolds number.

$$Nu = 2 + 0.459 Re^{0.55} Pr^{0.333} \quad (23)$$

The Drake correlation is similar in form to an earlier equation by Knudsen and Katz [30] with slightly different coefficients. The Reynolds number in Eq. (23) is the particle Reynolds number as defined in Eq. (11). The Drake correlation is intended for continuum flow and results in Nusselt number values larger than 2. However, the particle Knudsen numbers will typically be in the range of 0.1 – 2, meaning that the particles will experience transitional or possibly slip flow conditions. Using the Drake continuum correlation for Martian dust particles will over-estimate the Nusselt number and convective heating rate on the particle surface.

Fox, et al. [31] developed a Nusselt number correlation that accounts for compressible and non-continuum flow effects and is valid for subsonic and supersonic particle Mach numbers.

$$Nu = \frac{2\exp(-M)}{1+17\frac{M}{Re}} + 0.459Re^{0.55}Pr^{0.333} \left[\frac{1+0.5\exp(-17\frac{M}{Re})}{1.5} \right] \quad (24)$$

Kavanau and Drake [32] proposed a Nusselt number correlation intended for subsonic, compressible flows that is based on experimental wind tunnel data on spheres.

$$Nu = \frac{Nu^0}{1+3.42\frac{M}{RePr}Nu^0} \quad (25)$$

In Ref. [3], Papadopoulos, et al. use a Nusselt number correlation attributed to Eckert and Drake [30] that is similar in form to Eq. (25) and therefore presumably is also intended for subsonic particle Mach numbers.

$$\frac{Nu^0}{Nu} = 1 + \frac{\sqrt{2\pi\gamma^3}}{\gamma+1} \left(\frac{2-a}{a} \right) \frac{M}{RePr} Nu^0 \quad (26)$$

The value, Nu^0 , in Eqs. (25) and (26) is the Nusselt number for continuum flow, which can be evaluated using Eq. (23). For the surface accommodation coefficient, a , a value of 0.9 was used in Refs. [3] and [4].

Comparisons of the various Nusselt number correlations as a function of particle Reynolds number are shown in Fig. 8. A constant Prandtl number of 0.718 was assumed. Values for a constant subsonic particle Mach number of 0.5 are shown in Fig. 7a. As the particle Reynolds number approaches zero, the flow enters the free-molecular regime. At low Reynolds numbers, the continuum correlations predict a Nusselt number of 2, which is unrealistically high. The continuum model values increase from 2 as Reynolds number increases. The Fox, Kavanau, and Eckert correlations take into account compressibility and non-continuum effects. These correlations predict Nusselt numbers that approach zero at low Reynolds numbers. Increasing the Reynolds number for a constant value of Mach number drives the flow towards the continuum flow regime. For a particle Mach number of 0.5, the compressibility correlations approach the continuum values at Reynolds number values of around 100.

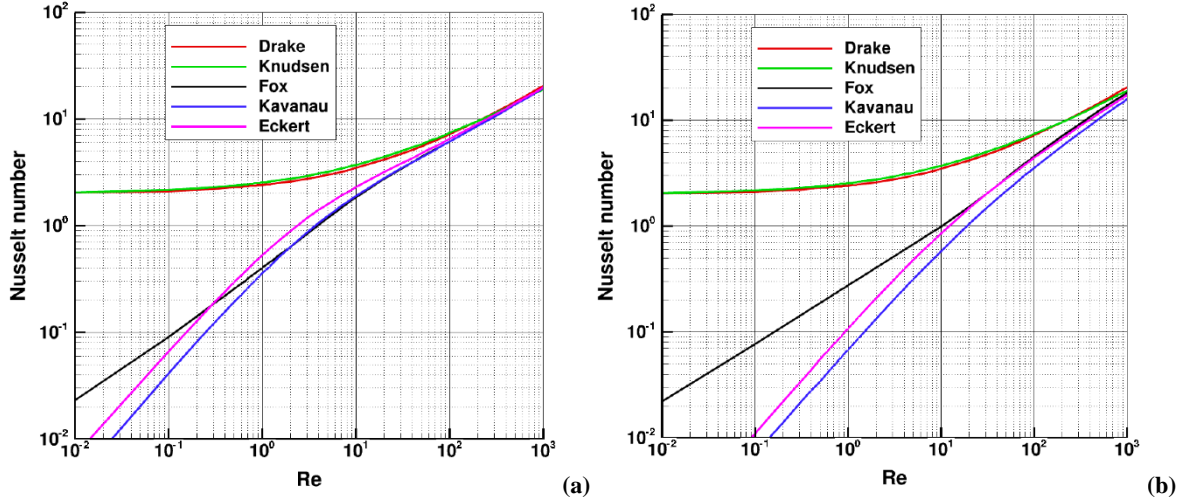


Fig. 8 Nusselt number correlation values as a function of Reynolds number (a) Mach = 0.5 (b) Mach = 3.0.

Results for a constant particle Mach number of 3.0 are shown in Fig. 8b. The continuum correlations of Drake and Knudsen are not a function Mach number, so the Mach 0.5 and 3.0 curves are the same. The Kavanau and Eckert correlations are designed for subsonic particle Mach numbers. When applied to a supersonic condition, they underpredict the Nusselt number values compared to the Fox correlation for particle Reynolds numbers less than 10. The Fox correlation is applicable for both subsonic and supersonic particle Mach numbers. As stated previously, values for the particle Reynolds number will typically be on the order of 1. Using the Kavanau or Eckert correlations for supersonic, low Reynolds number conditions will result in Nusselt numbers and heat transfer coefficients that are 2-3 times lower than values predicted by the Fox correlation.

Figure 9 shows predicted values of Nusselt number as a function of particle Mach number for a constant particle Reynolds number of 1. Increasing Mach number at a constant Reynolds number moves the flow away from the continuum regime. The continuum correlations are not a function of Mach number and show constant Nusselt number values of 2.41 and 2.54 along the entire Mach number range. As particle Mach number increases, the Fox correlation value converges asymptotically to a value of 0.274. The Kavanau and Eckert correlations are only applicable to subsonic Mach numbers, and they increasingly under-predict the Fox values as Mach number increases.

To summarize, based on expected values for particle Knudsen and Reynolds numbers, the flow around the particle will not be in the continuum flow regime, so the Drake or Knudsen correlations will over-estimate the Nusselt number. Because the dust particle Mach number will typically be supersonic, the subsonic Kavanau or Eckert correlations will tend to under-estimate Nusselt number. Of the Nusselt number correlations presented in this section, the best choice for Martian dust particle trajectory analysis appears to be the Fox correlation.

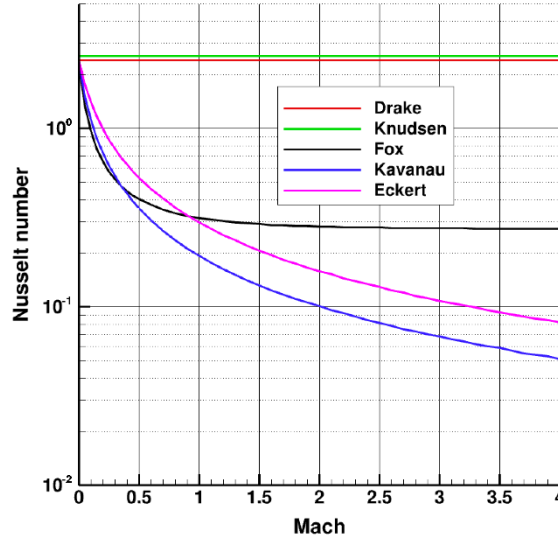


Fig. 9 Nusselt number correlation values as a function of particle Mach number, $Re = 1.0$.

D. Changes to Dust Particle Diameter

As dust particles travel through the shock layer, heat is transferred to the surface of the particle increasing the surface temperature. If the heat transfer is sufficiently high, the melting temperature will be reached. Martian dust particles are primarily SiO_2 , and the melting temperature of SiO_2 is approximately 1990 K. If additional energy is absorbed beyond the melting point, the surface temperature of the dust particle will continue to increase until the vaporization temperature is reached. At this point, gaseous material will be carried away from the surface of the particle, and the particle diameter will decrease.

Heatshield damage due to dust particle impacts is a function of the size of the particle at impact, so computing the change in the dust particle diameter as it travels through the shock layer can be (depending on the shock layer temperatures) an important part of the analysis. Previous work on Martian dust particle trajectory analysis has not included the effects of melt flow on the dust particles for reasons that are not explained, and this approach will be adopted in this study as well. Because dust particle melting is not considered, the particle will transition directly from a solid to gaseous state. Therefore, the process being modeled is sublimation rather than vaporization.

According to the approach used in this study, which is similar to that used in Ref. [3], once the vaporization temperature, T_{vapor} , is reached, any additional energy transfer to the surface of the particle will result in vaporization. The latent heat of vaporization, ζ , (referred to as the specific heat of vaporization in Ref. [3]) is the amount of energy required to change a unit mass of condensed material to gas at constant temperature. The rate of energy lost due to vaporization is set equal to the excess heat transfer beyond the vaporization temperature threshold over the surface area of the particle.

$$\zeta \frac{dm_p}{dt} = \zeta \rho_p \frac{dVol}{dt} = A_s C_h (T_g - T_{vapor}) \quad (27)$$

For spherical particles, the equation simplifies to the following:

$$\frac{d(d_p)}{dt} = \frac{2C_h(T_g - T_{vapor})}{\zeta\rho_p} \quad (28)$$

The latent heat of vaporization for SiO₂ is 8.6 MJ/kg. The heat transfer coefficient in Eq. (28) can be evaluated by relating it to the Nusselt number as previously discussed. To evaluate the change in particle diameter using Eq. (28), the vaporization temperature must be evaluated. The vaporization temperature occurs at the point at which the vapor pressure of a liquid material equals the ambient atmospheric pressure, allowing vapor to form and leave a liquid surface (or solid surface in the case of sublimation). The vapor pressure is the pressure exerted by a vapor in thermodynamic equilibrium with its condensed phases (i.e. solid or liquid) at a given temperature. The vaporization temperature increases with increasing surface pressure.

A number of models have been developed over the years to estimate the vaporization temperature of silicates. Centolanzi and Chapman [33] developed a correlation for the vaporization temperature of tektite, a naturally-occurring silicate glass that is used in Refs. [3] and [4]. The composition of tektite varies, but is approximately 70% SiO₂. Other significant components of tektite include Al₂O₃, MgO, and FeO. The Centolanzi and Chapman model expresses the vapor pressure as a function of temperature, but the correlation can be inverted to express the vaporization temperature as a function of the natural logarithm of surface pressure in atmospheres.

$$T_{vapor} = \frac{57400}{18.5 - \ln(p)} \quad (29)$$

Schaefer and Fegley [34] presented a different linear curve fit to the experimental data presented in Ref. [33] as a function of the common logarithm of the surface pressure in bars. Based on the figure in Ref. [34], the following equation was derived for the vaporization temperature of tektite glass.

$$T_{vapor} = 270 \log_{10}(p) + 3181 \quad (30)$$

A third approach to determine the vaporization temperature is by using an equilibrium chemistry solver, such as the Mutation++ code [35]. In this case, the condensed species of SiO₂ as well as the gaseous species, O, O₂, O₃, SiO, SiO₂, and Si are included in the chemical mixture. The equilibrium state of the mixture is computed by Mutation++ over a range of pressures. For a given pressure value, the temperature values are increased until gaseous species start to appear. This temperature is taken to be the vaporization temperature for SiO₂ at that pressure value.

A comparison of the various approaches to compute vaporization temperature is shown in Fig. 10. Also shown on the figure are isolated data points from the CRC Handbook of Chemistry and Physics [36] and Melosh [37]. At pressure values below 1 bar, the vaporization temperature values for SiO₂ computed by Mutation++ are similar to those predicted for tektite glass by the Schaefer and Fegley curve fit. The CRC Handbook value of 3220 K for SiO₂ at a pressure of 1 atm is similar to the Mutation++ and the Schaefer and Fegley values. The Centolanzi and Chapman curve fit has a different slope than the other data sources and is only close to them for pressure values around 0.1 bar. Due to its consistency with the other data sources, the Schaefer and Fegley curve fit was used in this study to estimate the vaporization temperature of the Martian dust particles.

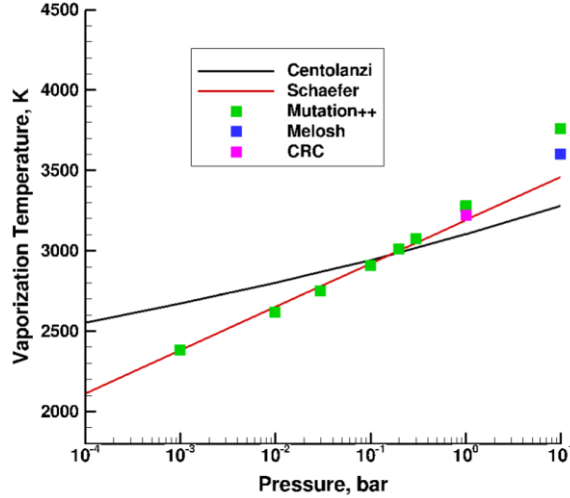


Fig. 10 Vaporization temperature of silicates as a function of pressure.

E. Particle Location

If a Lagrangian technique is used, equations to update the particle location are included in the set of coupled ODEs. The particle location equations are simply those that relate change in location to particle velocity.

$$\frac{d\vec{x}_p}{dt} = \vec{V}_p \quad (31)$$

Where:

$$\vec{x}_p = [x_p, y_p, z_p] \quad \text{and} \quad \vec{V}_p = [u_p, v_p, w_p]$$

F. Solving the Particle Trajectory Equations

The coupled set of ODEs that describe the motion of the dust particles through the shock layer can be solved using any applicable ODE solver. In this study, a standard 4th-order Runge Kutta approach was used. The particles were initialized at locations outside of the bow shock surrounding the vehicle. The initial particle velocities and temperatures were set to match freestream conditions. The ODEs are then integrated to update the particle trajectories as they travel through the shock layer until they either impact the heatshield or are carried around the heatshield and travel outside of the computational domain.

V. Surface Damage Models

A dust particle striking the heatshield with sufficient kinetic energy will cause spallation damage to the TPS material. In addition to particle kinetic energy, the composition, density, and strength of both the particle and the heatshield are factors in how much damage a particle impact will cause. Surface damage correlations, when possible, should be based on experimental data. The experimental data described in this section measured either the impact crater diameter and penetration depth from a single particle impact or the overall mass loss of the test material due to cumulative dust particle impacts during the test. Existing experimental data from the Apollo- and Shuttle-era was based on projectile sizes of 0.4 mm or larger, which is two orders of magnitude larger than Martian dust particles. Other experimental data on cork and Norcoat Liège used particle sizes ranging from 0.5 to 50 micron, values that are more consistent with the size of Martian dust.

In this section, surface damage correlations will be presented for five materials: fused-silica, AVCOAT, Space Shuttle tiles, cork, and Norcoat Liège. Previous work on impact cratering [38] suggest that the crater diameter is proportional to the cube root of the particle kinetic energy. This scaling relationship was found to be approximately valid over orders of magnitude of both energy and particle size, and several of the surface damage correlations presented in this section are based on this scaling. One thing to be careful of when assessing and making use of the

legacy surface damage equations is they are often inconsistent with regards to units, often using both CGS and SI (and sometimes other) units in the same equation. In this study, all of the correlations are presented based on MKS units.

A. Fused-Silica

A series of experiments were performed at the Manned Space Center (MSC) in Houston during the Apollo program that involved firing spherical projectiles at fused-silica targets [39]. The motivation of the experiments was to generate experimental data to assess the damage caused by micro-meteor impacts on the windows of the Apollo spacecraft. Papadopoulos, et al. [3] claimed that this experimental data could be applied to TPS materials such as FRCI-12 tiles used on the Space Shuttle. These tiles have a 0.35 mm thick tetraborosilicate, black, glassy surface. The projectiles used in the MSC experiments were spheres made from Pyrex, aluminum, and sapphire with diameters ranging from 0.4 to 1.58 mm. The spheres were fired at semi-infinite (i.e. flat) fused silica targets in the ballistic range at the MSC at velocities ranging from 170 to 7480 m/s.

For spherical particles of uniform composition, the kinetic energy can be expressed in terms of the particle density, diameter, and velocity.

$$K.E. = \frac{\pi}{12} \rho_p d_p^3 V_p^2 \quad (32)$$

Based on this relationship to kinetic energy, Papadopoulos, et al. [3] derived a correlation for impact crater diameter in fused-silica as a function of particle diameter and velocity.

$$D_c = 0.113 d_p v_p^{2/3} \quad (33)$$

Equation (33) was based on the Pyrex projectile data from Ref. [39], because Papadopoulos, et al. felt that Pyrex was the closest in composition to the silica-based Martian dust particles. A particle density term is not included in Eq. (33), so it is likely that Papadopoulos, et al. incorporated the density of Pyrex, 2230 kg/m³, into the leading coefficient. Since Martian dust particles are not made from Pyrex and will therefore have a different density, Eq. (33) was recast to include the particle density to the 1/3 power.

$$D_c = 0.00865 \rho_p^{1/3} d_p v_p^{2/3} \quad (34)$$

The experimental crater diameter data from Ref. [39] as a function of particle kinetic energy is shown in Fig. 11. The original leading coefficient value of 0.00865 for the Papadopoulos, et al. correlation overestimates the impact crater diameter compared to most of the experimental data. Martian dust particles will have diameters on the order of microns, so the kinetic energy for Martian dust will be at the low end of the values shown in Fig. 11. If the leading coefficient of Eq. (34) is adjusted to a value of 0.006, it provides a better fit to the experimental data for lower values of particle kinetic energy.

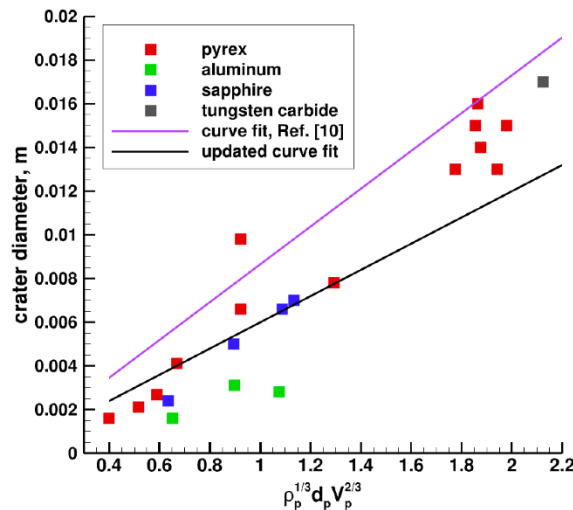


Fig. 11 Crater diameter for projectiles fired into fused silica targets.

The impact penetration (i.e. crater) depth data from Ref. [39] does not correlate to the cube root of particle kinetic energy. Flaherty [39] presents the Manned Space Center (MSC) glass penetration equation that is based on impact tests into fused silica performed at the MSC during the Apollo program.

$$p = 2.21 \times 10^{-4} \rho_p^{0.5} d_p^{1.06} v_p^{0.667} \quad (35)$$

The original form of the MCS penetration equation as presented in Ref. [39] used a mixture of CGS and MKS units. The leading coefficient shown in Eq. (35) is the value assuming all of the elements in the MSC equation are converted to MKS units. According to Flaherty [39], the crater depth correlation shown in Eq. (35) is applicable for projectiles 400 μm in diameter or larger (two orders of magnitude larger than Martian dust particles).

Papadopoulos, et al. [3] derived an alternative equation for crater penetration depth in fused-silica targets based on the Flaherty data for Pyrex projectiles.

$$p = 0.3016 d_p^{1.4} v_p^{0.667} \quad (36)$$

As was done with the crater diameter correlation, the Papadopoulos, et al. penetration equation shown in Eq. (36) appears to have the density of Pyrex incorporated into the leading coefficient. If the equation is recast using the square root of particle density, the scaling factor used in the MSC equation, the Papadopoulos, et al. equation becomes:

$$p = 0.00639 \rho_p^{0.5} d_p^{1.4} v_p^{0.667} \quad (37)$$

The crater penetration depth predicted by Eq. (37) compared to the experimental data is shown in Fig. 12. The values computed by the MSC equation are not shown on the figure, but consistently under-estimate the experimental data by a factor of 2 or more. The original leading coefficient of 0.00639 from Ref. [3] also under-estimates most of the experimental data. Adjusting the value of the leading coefficient to a larger value of 0.01 increases the predicted crater depth and improves the correlation with the experimental data.

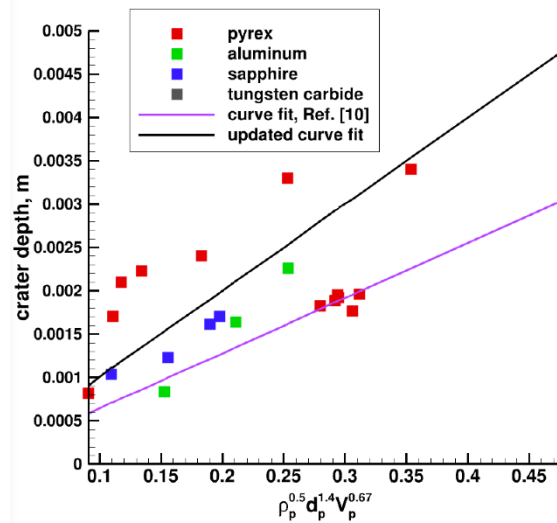


Fig. 12 Crater depth for projectiles fired into fused silica targets.

B. AVCOAT

A correlation similar in form to the MSC glass penetration equation was developed for hypervelocity impact into AVCOAT, the TPS material used in the Apollo heatshield [40]. The data was presumably taken in the ballistic ranges at MSC, because the form of the correlation is similar to the glass penetration equation for fused-silica. For the AVCOAT tests, 1.59- and 3.17-mm diameter spheres made from glass and nylon were fired at AVCOAT targets at velocities ranging from 4 to 8 km/s. As was the case with the MSC glass penetration equation, the penetration depth is a function of the particle diameter, density, and velocity at impact. The AVCOAT equation presented in Ref. [40]

uses mixed CGS and MKS units. If the particle diameter, density, and velocity are all expressed in MKS units, the equation for penetration depth in meters becomes the following:

$$p = 7.09 \times 10^{-4} \rho_p^{0.5} d_p^{1.06} v_p^{0.667} \quad (38)$$

Comparing Eqs. (35) and (38), the predicted impact crater penetration depth into AVCOAT should be about three times that for fused-silica all other inputs being equal. AVCOAT is a charring ablative material, and Eq. (38) is based on experiments using virgin AVCOAT. If the material is ablating during re-entry, there will be layer of charred material at the surface. To account for the increased damage particle impacts will cause to charred material, Papadopoulos, et al. [3] came up with a penetration depth equation for charred AVCOAT.

$$p = 5 \times 10^{-4} \rho_p^{0.5} d_p v_p^{0.667} \quad (39)$$

Note that in Eq. (39) the exponent on the particle diameter has changed from 1.06 to 1. The form of the charring AVCOAT equation presented in Ref. [3] is different, because the density of the glass projectiles, 2300 kg/m^3 , has been pulled into the leading coefficient. No information was given in Ref. [40] for the impact crater diameter in AVCOAT. Papadopoulos, et al. [3] assumed a hemi-spherical crater shape for both virgin and charred AVCOAT, so the crater diameter is simply twice the penetration depth.

C. Space Shuttle Tiles

Christiansen and Ortega [41] published results from 22 hypervelocity impact tests performed at the NASA JSC Hypervelocity Impact Research Laboratory (HIRL). The targets were LI-900 (density = 140 kg/m^3) and LI-2200 (density = 350 kg/m^3) Space Shuttle TPS tiles. In 19 of the 21 tests, the surface of the tiles was coated with a 0.381 mm thick layer of borosilicate glass. The other two tests used uncoated tiles. The projectiles fired at the tiles were spheres and cylinders made from aluminum (density = 2800 kg/m^3) and nylon (density = 1140 kg/m^3). The sphere diameters ranged from 0.79 – 3.59-mm. Velocities ranged from 4.43 – 7.12 km/s.

Based on the experimental data, a correlation was derived for impact crater diameter in the LI-900 and LI-2200 tiles as a function of particle diameter, density, and velocity.

$$D_c = 0.00185 \rho_p^{1/3} d_p v_p^{2/3} (1 + 0.25 \sin \theta)^{2/3} \quad (40)$$

Equation (40) includes a term representing the impact angle, θ , relative to the surface normal. The same crater diameter equation is applied to both LI-900 and LI-2200 tiles. The correlation shown in Eq. (40) is consistent with the premise that impact crater diameter is proportional to the cube root of particle kinetic energy. The leading coefficient in Eq. (40) corresponds to all of the elements in the equation expressed in MKS units. A different leading coefficient was presented in Ref. [41] that was based on a mixed system of units (mm for the lengths, gm/cm^3 for the density, and km/s for the velocity).

Based on the LI-900 and LI-2200 tile experimental data, a correlation was derived for impact crater penetration depth that includes terms for the density of the target material, ρ_t , as well as the impact angle [41].

$$p = 0.0127 \left(\frac{\rho_p}{\rho_t} \right)^{1/2} d_p (v_p \cos \theta)^{2/3} \quad (41)$$

Equation (41) predicts a relatively high penetration depth compared to the fused-silica and AVCOAT models, particularly for the LI-900 tile where the penetration depth can be several times larger than the particle diameter. This situation probably reflects that once the particle breaks through the 0.381-mm thick borosilicate coating there is relatively little resistance to further penetration into the low-density LI-900 material.

D. Cork

Lorenz [42] presented data taken in the Boeing 12-inch diameter hypersonic wind tunnel in the late 1960s to determine the erosion effects caused by sand and glass particles impacting with heated ablative materials. The smallest particles used in the series of experiments, 50-micron diameter spherical glass beads, are closer in size to Martian dust particles than the particles used in the fused-silica, AVCOAT, or Shuttle tile data discussed previously. The flow velocity in the test section was between 1160 – 1225 m/s. The 50-micron glass particles reached a velocity of approximately 990 m/s (3250 ft/s). The models exposed to the dusty flow were 0.046 m diameter (1.8 in) hemispheres

and blunted cones. Three materials were used for the models: cork, silicone rubber, and carborazole. The focus in this paper will be on the cork data.

The particle erosion data in Ref. [42] is presented in terms of total mass loss of the model due to all particle impacts over the test time as a function of mass of the impinging particles. For example, in one of the test runs from Ref. [42], a total mass of 4 gm of impinging 50-micron glass particles resulted in a model mass loss of approximately 5 gm. Assuming spherical glass particles with a diameter of 50-micron and a density of 2300 kg/m³, the mass loss of cork due to a single glass particle impact can be estimated.

In order to derive an equation for impact crater diameter for cork, several assumptions are made. The crater diameter is assumed to be a function of the cube root of particle kinetic energy. A hemispherical crater shape is assumed. The total surface erosion was assumed to be the cumulative total of the individual particle impacts. The effect of impact angle on the model is ignored. Lorenz states in Ref. [42] that there was particle stratification in the tunnel flow, an effect that is also ignored.

Using all of these assumptions and based on data corresponding to a surface temperature of 727 K, an approximate correlation was derived for the impact crater diameter in cork.

$$D_c = 0.0027\rho_p^{1/3}d_p v_p^{2/3} \quad (42)$$

Because the impact craters are assumed to be hemispherical, the crater penetration depth is simply one-half the crater diameter.

$$p = 0.00135\rho_p^{1/3}d_p v_p^{2/3} \quad (43)$$

E. Norcoat Liège

Norcoat Liège is a charring, ablative TPS material that was used on the heatshield of the ExoMars Schiaparelli capsule that entered the Martian atmosphere in 2016 [43]. It consists of cork particles infused with phenolic resin and has a density of 470 kg/m³. A series of hot erosion tests were performed in the German Aerospace Center (DLR) L2K arcjet facility to assess the surface erosion due to dust particle impacts in Norcoat Liège [43]. The test articles were 0.1m diameter, flat, circular disks of Norcoat Liège. The models were exposed to heating rates ranging from 15-45 W/cm² for test times of 90 and 145 seconds. The L2K test facility had the ability to inject particles made from boron nitride (BN) and Al₂O₃ into the flow to measure material erosion due to dust particle impacts. Particle diameters used in the experiments ranged from 0.5 to 15 microns, which is consistent with the size of Martian dust particles. The models were weighed before and after the test to determine the total mass lost during the test time.

The Norcoat Liège samples experienced thermochemical ablation during the experiments. A series of preliminary tests were performed without dust insertion at various heating rates and test duration times to quantify the level of mass loss due to thermochemical ablation alone. These tests were then repeated with dust particles inserted into the flow. Based on this experimental data, a correlation was presented in Ref. [43] for total mass loss due to thermochemical ablation and dust particle impacts.

$$\Delta m_a = \Delta m_{ref} + 2.16 \times 10^{-8} v_p^2 d_p^{3.146} \rho_p^{1.86} \Delta M_p \quad (44)$$

The quantity, Δm_a , in Eq. (44) is the total mass lost during the test time. The estimated amount of mass loss due to thermochemical ablation is Δm_{ref} . The other terms on the right-hand side of Eq. (44) represent the total mass loss from surface erosion due to particle impacts. The quantity, ΔM_p , is the total number of particles that impacted the model during the test. As presented in Ref. [43], the equation uses a mixed system of units (mass in grams, MKS for everything else).

In order to derive an expression for the impact crater diameter from a single particle impact, several assumptions are made. The crater shape is assumed to be hemispherical. The total mass loss due to particle impacts measured during the test is assumed to be equal to the sum of the individual particle impacts. The impact angle is assumed to be zero, which is reasonable since a flat-face test article was used. With these assumptions, impact crater diameter for a particle impact into Norcoat Liège can be expressed as a function of the particle diameter, velocity, and density at impact.

$$D_c = 0.00056\rho_p^{0.62}d_p^{1.04867}v_p^{0.667} \quad (45)$$

In Eq. (45), the density of Norcoat Liège, 470 kg/m³, has been incorporated into the leading coefficient. Note that the exponents in Eq. (45) don't follow the convention of scaling the crater diameter with the cube root of particle kinetic energy. With hemispherical craters, the penetration depth is one-half the crater diameter.

$$p = 0.00028\rho_p^{0.62}d_p^{1.04867}v_p^{0.667} \quad (46)$$

F. Comparisons of Impact Crater Diameter and Depth

To compare the impact damage correlations for the various materials presented in this section, the impact crater diameter and penetration depth are plotted as a function of impact velocity in Fig. 13. The curves are based on a 5-micron diameter particle with a particle density of 2940 kg/m³. Fused-silica has the largest crater diameter and smallest crater depth indicating a shallow impact crater that is consistent with fused-silica being a hard, brittle material. The LI-900 and LI-2200 tile use the same correlation for crater diameter, so the two curves are identical. The LI-900 tile has the lowest density of any of the materials in the figure and allows the greatest crater penetration depth. Interestingly, Norcoat Liège offers slightly worse damage resistance than pure cork in that the predicted crater diameter and penetration depth for Norcoat Liège are slightly larger. However, the cork correlations were based on one experimental velocity, so the uncertainty in the cork correlations presented earlier in this section may be quite high. Both virgin and charred AVCOAT curves are included in Fig. 13. According to these approximate surface damage models, the impact resistance of Norcoat Liège lies somewhere in between virgin and charred AVCOAT.

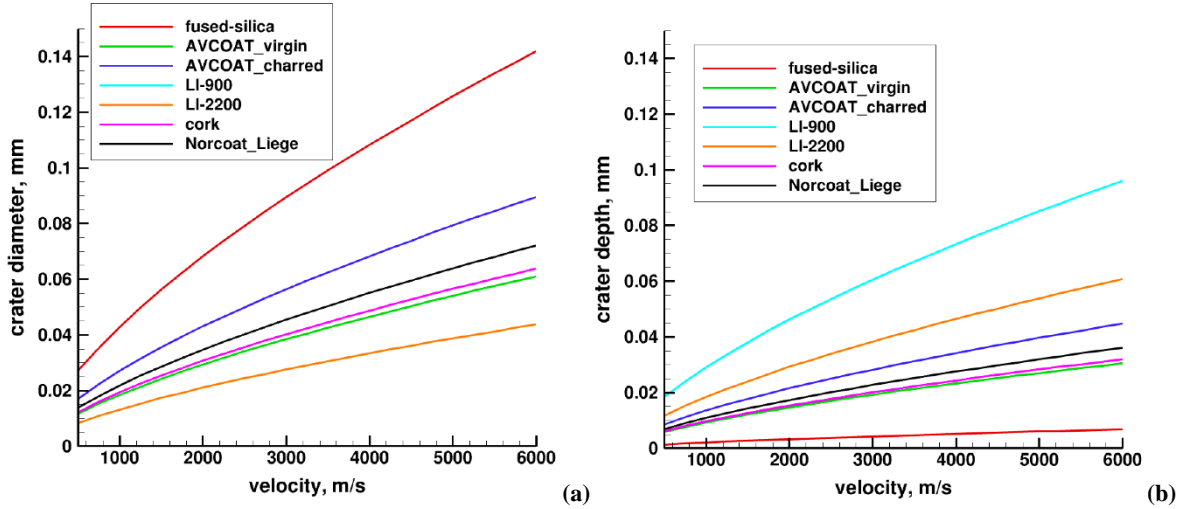


Fig. 13 Surface damage predictions for various TPS materials. (a) impact crater diameter (b) crater penetration depth.

VI. Shock Layer Flow Solution

As stated previously, the particle trajectories will be altered by the flow in the shock layer, so flow solutions must be generated at a number of points along the entry trajectory. With one-way particle-fluid coupling, an “off the shelf” CFD code can be used to compute the shock layer flow solutions along the entry trajectory as long as the CFD code has the necessary physical model capability to capture the finite-rate chemical reactions and other effects that will occur in the shock layer. With two-way particle-fluid coupling, the particles and fluid will exchange momentum and energy. In this case, the governing equations solved by the CFD code must include a source term vector, I , that represents the influence of the particles on the gas flow.

$$\frac{\partial u}{\partial t} + \vec{\nabla} \cdot F = -I \quad (47)$$

For the 1-D flow equations, the particle source term vector represents contributions from the particles to the conservation of mass, momentum and energy equations for the fluid.

$$I = \begin{bmatrix} 0 \\ \sum_{i=1}^N n_i F_{D,i} \\ \sum_{i=1}^N n_i (F_{D,i} \cdot v_i + H_i) \end{bmatrix} \quad (48)$$

The term, $F_{D,i}$, is the drag force on a single particle of diameter, i , as defined by Eq. (8). The summation is performed for all of the discrete particle diameter values present in the simulation and accounts for the fact that drag force is a function of particle diameter. The term, n_i , is the number density of particles with diameter, i . The convective heat transfer over the surface of a particle, H_i , makes use of the Nusselt number definition as was done in Section IV.

$$H_i = \pi d_p^2 C_h (T_g - T_p) = \pi d_p \kappa_g Nu (T_g - T_p) \quad (49)$$

For 2-D or 3-D simulations, the drag force terms in the momentum equations would be multiplied by direction cosines corresponding to the direction of the relative velocity vector. Depending on the level of modeling complexity, other force terms might appear in the source term vector in addition to that of drag force. For example, thermophoretic force caused by a temperature difference on either side of a particle might be included.

VII. Material Response Code

The TPS for a planetary entry vehicle is typically sized by performing a material response simulation along the entry trajectory. For ablating TPS materials such as PICA [44] or Norcoat Liege [43], the surface energy balance solved by the material response code will include the effects of energy loss due to charring ablator and pyrolysis gas flow. The surface recession is equal to the charring ablator mass flux divided by the material density. For entry into Mars, this surface recession will be augmented by the damage caused by dust particle impacts.

In this study, the Icarus material response solver [45] was used to model the heatshield material response. Icarus [45] is a three-dimensional, unstructured code developed at NASA Ames that solves the finite-volume formulation of the material response equations including the effects of material decomposition and ablation. The code has previously been applied to planetary entry simulations including Huygens vehicle during its entry into the atmosphere of Titan [46]. A surface erosion boundary condition has been implemented in Icarus that solves a surface energy balance that includes the effects of charring ablator mass flow, pyrolysis gas flow, and surface ablation due to particle impacts. The surface erosion inputs into Icarus are the particle diameter, velocity, and number of particles per unit area striking the heatshield. These inputs can be both time- and spatially-varying.

VIII. Results

In order to demonstrate the one-way coupling approach, this method was applied to compute the theoretical dust erosion on the ExoMars Schiaparelli capsule [47] during its October 2016 descent into the Martian atmosphere. The Schiaparelli entry capsule (a 2.4 m diameter, 70-deg sphere cone) included a tiled Norcoat Liège heatshield is shown in Fig. 14. One of the mission goals of Schiaparelli was to enter the Martian atmosphere during a time of year when dust storms are more likely to occur in order to (hopefully) perform atmospheric and surface measurements in the dust-rich environment. Unfortunately, a dust storm did not occur when Schiaparelli began its descent, but detailed trajectory information on the Schiaparelli entry is available to perform a dust erosion analysis.



Fig. 14 Schiaparelli heatshield.

In order to provide the flow solutions necessary for the particle trajectory analysis, 3-D CFD solutions were generated at 10 trajectory points using the DPLR Navier-Stokes flow solver [47]. For the Schiaparelli solutions, an 8-species [CO₂, CO, N₂, O₂, NO, C, N, O] finite-rate chemistry model was used. Thermochemical non-equilibrium was simulated using a two-temperature (T-Tv) model. A fully-catalytic, radiative equilibrium wall boundary condition was used. The CFD approach used in this study is similar to that employed by Brandis, et al. [48] when they compared CFD results against Schiaparelli aerothermal flight data.

The CFD trajectory points are shown in Table 5. The five lowest altitude points are known in the literature [49] as Schiaparelli trajectory points S2 through S5. In addition to these trajectory points, five additional, higher-altitude points were selected at 5 km intervals up to an altitude of 50 km.

Table 5. Schiaparelli CFD trajectory points.

Altitude, km	Density, kg/m ³	Velocity, m/s	Temperature, K	Angle of attack, deg
50.0	1.755e-4	5500.6	171.8	7.2
45.0	2.944e-4	5185.0	175.0	7.2
40.0	4.825e-4	4689.0	182.4	7.2
35.0	7.717e-4	4016.9	186.3	7.2
30.0	1.322e-3	2913.7	190.1	6.0
28.2	1.542e-3	2595.4	191.6	5.8
25.5	1.979e-3	2013.8	195.4	5.0
23.1	2.440e-3	1570.6	199.1	4.2
20.9	2.962e-3	1236.9	202.3	3.0
18.9	3.478e-3	1001.9	205.8	3.0

The Schiaparelli entry trajectory is relatively benign in terms of heating rate with a peak stagnation point convective heating rate of about 45 W/cm² at 45 km altitude. Once the CFD solutions were complete for the 10 trajectory points, the required flow data (density, velocity, temperature, thermal conductivity, etc.) was extracted on the symmetry plane to provide the underlying shock layer fluid data required by the 2-D particle trajectory code.

In this study, particle trajectory simulations were performed for the three dust environment conditions described in Section III. The first dust condition corresponded to the 2007 global dust storm. This environment had the highest dust loading of the three conditions analyzed. The second dust condition was taken during the 2012 regional dust storm, and the third simulation was for the relatively quiet dust conditions seen prior to the 2012 regional dust storm. For each dust environment, the particle trajectory code was run at each of the CFD trajectory points for each of the 15 particle diameter values shown in Fig. 3. In order to get a distribution of particle diameters and velocities along the surface, particle trajectories were computed at evenly-spaced starting locations along the outer boundary of the CFD grid. The particle trajectory code then updated the particle location and state by solving the set of coupled ODEs

described in Section IV until the particle either struck the surface or was deflected around the heatshield. In certain situations where the freestream velocity was low, the particle would slow down enough so it would be “captured” by the boundary layer and never reach the surface. In this case the particle trajectory simulation was halted after a sufficiently long simulation time.

Smaller particles are slowed down and deflected more by the surrounding flow than are larger particles, and the surface temperature of the smaller particles reaches higher levels due to the increased surface heating rate. An example of the trajectories of small particles is shown in Fig. 15 where six 1-micron diameter particles starting at different locations along the outer boundary of the CFD grid travel through the shock layer at 30 km altitude. The circles represent particle location, and the color inside the circle denotes the particle velocity. In this situation, most of the 1-micron particles are deflected enough by the flow that they miss the heatshield. In contrast, when 5-micron diameter particles are simulated, the deceleration and deflection is greatly reduced, and every particle except the one started at the $y = -1.25$ location strikes the heatshield.

For the Schiaparelli simulation, the 1-micron diameter particles experience the highest surface temperature increase. The peak temperature is slightly less than the vaporization temperature. Changes to the entry trajectory (i.e. making it steeper) or to assumptions that go into the heat transfer coefficient or material properties might cause the smaller particles to exceed the vaporization temperature, but for the results presented in this paper all of the particles maintained their original size.

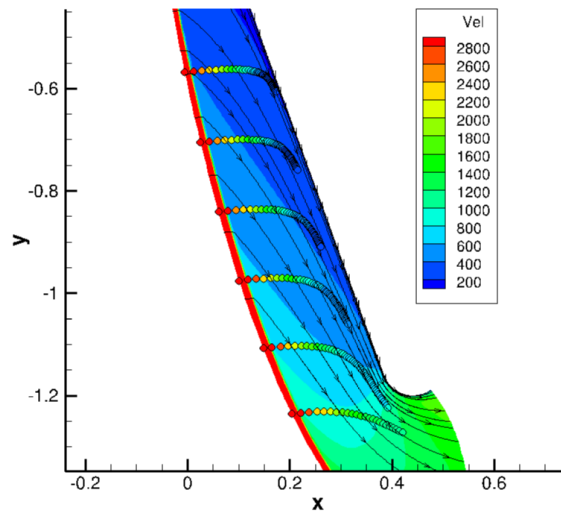


Fig. 15 Trajectories of 1-micron diameter particles through the shock layer, 30-km altitude.

The particle impact velocity on the heatshield is a function of particle size and the initial particle location in the shock layer. Figure 16 show impact velocities as a function of particle size at the 35 km trajectory point. The freestream velocity at this trajectory point is 4017 m/s. The x-axis represents vertical location along the symmetry plane of the capsule with the center of the heatshield at $y=0$. Along the stagnation line, close to $y=0$, the shock layer is thinnest, so the particles pass through the shock layer relatively quickly with less time to decelerate into the fluid. As the initial particle location moves away from the stagnation line, the shock layer is thicker, so the particles slow down to a greater extent. The amount of deceleration is a function of the particle size. Particles with diameters equal to or greater than 9 microns experience very little deceleration and strike the heatshield at close to the freestream velocity. The asymmetry in Fig. 16 is due to the slight angle of attack experienced by the Schiaparelli entry capsule.

The Schiaparelli heatshield consisted of Norcoat Liège insulating tiles, but properties for this TPS material are not currently available in the Icarus material database. For the Schiaparelli dust erosion analysis, PICA was used to approximate the heatshield material in the Icarus simulations. The switch to PICA affects the amount of surface recession due to thermochemical (charring) ablation predicted by Icarus but has no effect on the amount of dust particle erosion because the surface damage models for Norcoat Liege were used in the simulation, and they are only a function of particle number density, diameter, and impact velocity.

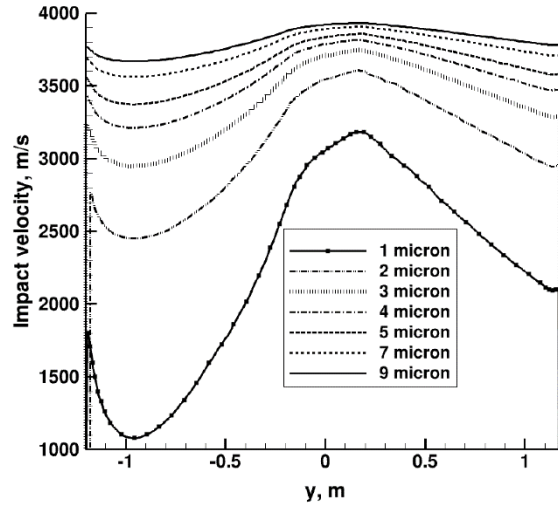


Fig. 16 Impact velocity as a function of particle size, 35-km trajectory point.

Using inputs provided by the particle trajectory code, the Icarus code computed the material response of the Schiaparelli capsule along its entry trajectory from 50 to 18 km altitude. The surface damage correlations for Norcoat Liège shown in Eqs. (45) and (46) were used to compute impact damage. The largest dust surface erosion occurs at the stagnation point where the particle deceleration is the smallest. The recession rate at the stagnation point due to dust particle impacts for the 2007 dust storm condition as a function of dust particle diameter is shown in Fig. 17. The greatest rate of surface recession is caused by the 4- and 5-micron diameter particles, followed by the 3- and 6-micron particles. There are fewer of the larger diameter particles, but each one does significantly more damage than do the smaller particles. The 1-micron diameter particles, even though they are the most numerous, do relatively little damage to the heatshield. The maximum rate of dust erosion recession occurs at the 35 km trajectory point, which corresponds to the location on the entry trajectory of peak dynamic pressure

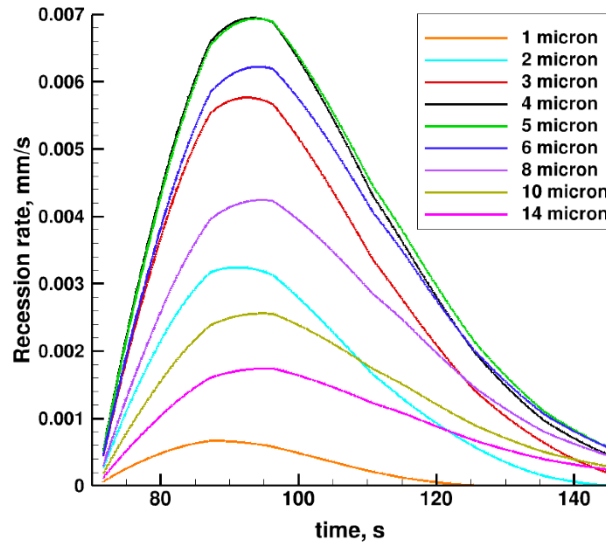


Fig. 17 Rate of surface recession due to dust particle impacts as a function of particle diameter, 2007 dust condition.

Along with the surface recession due to dust particle impacts, the Icarus code also predicted the recession due to charring ablation of the PICA heatshield between 50 and 18 km altitude. The cumulative recession for both char and dust impact erosion for all three dust conditions as a function of time are shown in Fig. 18. The majority of the char

recession occurs at altitudes above 30 km. The value of char recession asymptotes out after this point to a value of about 2.6 mm. Due to the conflicting trends of increasing mass mixing ratio and decreasing freestream velocity, there is still significant dust erosion at altitudes of 23-25 km. The 2007 dust condition was the most severe corresponding to a major global dust storm. The cumulative dust particle impact recession for the 2007 condition was 2.1 mm, which is 80% of the value due to thermochemical ablation. The design TPS thickness for the Schiaparelli entry vehicle was 12.4 mm [50], so 2.1 mm would consume 17% of the heatshield thickness. The dust condition corresponding to the November 2012 regional dust storm was less severe, and generated a total surface recession at the stagnation point of 0.35 mm. The heatshield erosion during the quiescent dust condition from October 2012 was negligible at only 0.04 mm.

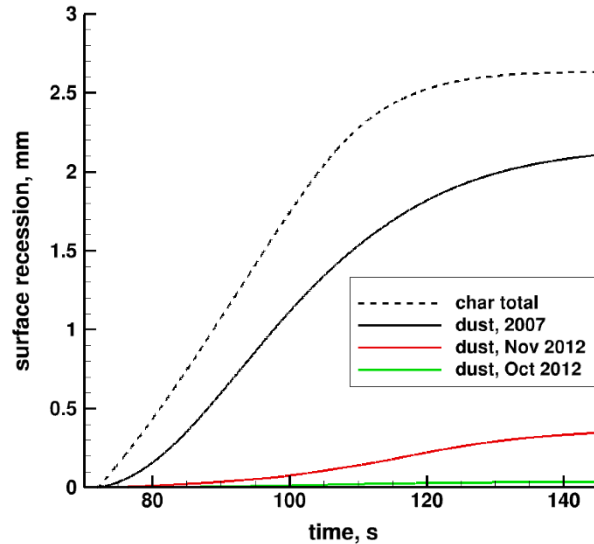


Fig. 18 Total surface recession due to charring ablation and dust particle impacts.

IX. Conclusions

One of the unique challenges of designing a vehicle that will enter into the Martian atmosphere is the presence of dust that can cause surface erosion of the heatshield of the vehicle. The dust environment can vary widely depending on whether regional or global dust storms are present, and the timing of these storms is unpredictable. This paper provided an overview of the equations and modeling assumptions that go into an analysis of the heatshield erosion due to dust particle impacts for a spacecraft entering the Martian atmosphere. The equations for determining the dust loading in the atmosphere based on observations from the MCS were presented. The different levels of fidelity in terms of particle-fluid coupling were discussed.

The equations for determining the dust particle trajectories as they travel through the shock layer that surrounds the heatshield using the Lagrangian framework were presented. The importance of including non-continuum effects when calculating dust particle drag coefficient and heat transfer coefficient were discussed. When particles strike the heatshield surface, the spallation damage they cause is a function of TPS material as well as the particle diameter, density, and impact velocity. Surface damage correlations were presented for five TPS materials – fused-silica, AVCOAT, Space Shuttle tiles, cork, and Norcoat Liège.

The one-way coupling approach described in this paper was applied to compute the heatshield erosion due to thermochemical ablation and dust particle impacts for the Schiaparelli entry vehicle along its 2016 entry trajectory. Based on MCS data, the dust erosion analysis was performed at three different dust conditions – during the 2007 global dust storm, the November 2012 regional dust storm, and during quiescent dust conditions from October 2012. The most severe 2007 dust environment resulted in a predicted heatshield erosion at the stagnation point of 2.1 mm, which was comparable to the recession caused by thermochemical ablation and equal to 17% of the design TPS thickness. Heatshield erosion due to dust particle impacts at the more benign November 2012 regional dust storm was only 0.35 mm, and it was negligible during quiescent dust conditions.

Acknowledgments

Support for this work was provided by the Entry Systems Modeling (ESM) project under the NASA Game Changing Development (GCD) program. Support for Grant Palmer was provided under NASA contract NNA15BB15C to AMA, Inc.

References

- [1] Zurak R. W., "Martian Great Dust Storms: An Update", *Icarus*, 32, 288-310, 1982.
- [2] Toon, O.B., Pollack, J.B., and Sagan, C., "Physical Properties of the Particles Composing the Martian Dust Storm of 1971-1972," *Icarus*, Vol. 30, 1977, pp. 663-696.
- [3] Papadopoulos, P., Tauber, M., and Chang, I-D., "Heat Shield Erosion in a Dusty Martian Atmosphere", *Journal of Spacecraft and Rockets*, Vol. 30, No. 2, 1993, pp. 140-151.
- [4] Palmer, G., Chen, Y.-K., Papadopoulos, P., and Tauber, M., "Reassessment of Effect of Dust Erosion on Heatshield of Mars Entry Vehicle," *Journal of Spacecraft and Rockets*, Vol. 37, No. 6, Nov 2000, pp. 747-752.
- [5] Elangovan, R. and Cao, H.V., "Dusty Supersonic Viscous Flow over a Two-Dimensional Blunt Body," *J. of Thermophysics and Heat Transfer*, Vol. 4, No. 4, 1990, pp. 529-532.
- [6] Saito, T., Marumoto, M., and Takayama, K., "Numerical Investigations of Shock Waves in Gas-Particle Mixtures," *Shock Waves*, Vol. 13, 2003, pp. 299-322.
- [7] Marois, G., Villedieu, P., and Mathiad, J., "Euler-Euler Modelling of the Interaction of a Gas-Particle Mixture with a Detached Shock," 13th World Congress on Computational Mechanics, 2018.
- [8] Ching, E., Brill, S., Lv, Y., and Ihme, M., "Development of a Lagrangian Particle Tracking Method for High-Order Discontinuous Galerkin Schemes," AIAA Paper 2018-0360, Jan. 2018.
- [9] Ching, E. and Ihme, M., "Sensitivity study of high-speed dusty flows over blunt bodies simulated using a discontinuous Galerkin method," AIAA Paper 2019-0895, Jan. 2019.
- [10] Metzger, S.M., Carr, J.R., Johnson, J.R., Parker, T.J., and Lemmon, M.T., "Dust devil vortices seen by the Mars Pathfinder camera," *Geophys. Res. Letters*, Vol. 26, No. 18, 1999, pp. 2781-2784.
- [11] Heavens, N., Johnson, M., Abdou, W., Kass, D., Kleinbohl, A., McCleese, D., Shirley, J., and Wilson, R., "Seasonal and diurnal variability of detached dust layers in the tropical Martian atmosphere," *J. of Geophys. Res.: Planets*, 119, 2014, pp. 1-27.
- [12] Petty, G.W. and Huang, W., "The Modified Gamma Size Distribution Applied to Inhomogenous and Nonspherical Particles: Key Relationships and Conversions," *J. of the Atmos. Sciences*, Vol. 68, 2011, pp. 1460-1473.
- [13] Heavens, N., Richardson, M., Kleinbohl, A., Kass, D., McCleese, D., Abdou, W., Benson, J., Schofield, J., Shirley, J., and Wolkenberg, P., "The vertical distribution of dust in the Martian atmosphere during northern spring and summer: Observations by the Mars Climate Sounder and analysis of zonal average vertical dust profiles," *J. of Geophys. Research*, Vol. 116, 2011, pp. 1-23.
- [14] Tomasko, M.G., Doose, I.R., Lemmon, M., Smith, P.H., and Wegryn, E., "Properties of dust in the Martian atmosphere from the Imager on Mars Pathfinder," *J. of Geophys. Research*, Vol. 104, No. E4, 1999, pp. 8987-9007.
- [15] Kahre, M.A., Hollingsworth, J.L., Haberle, R.M., and Murphy, J.R., "Investigations of the variability of dust particle sizes in the Martian atmosphere using the NASA Ames General Circulation Model," *Icarus*, Vol. 195, 2008, pp. 576-597.
- [16] Chen-Chen, H., Perez-Hoyos, S., and Sanchez-Lavega, A., "Dust particle size and optical depth on Mars retrieved by the MSL navigation cameras," *Icarus*, Vol. 319, 2019, pp. 43-57.
- [17] Wolff, M.J. and Clancy, R.T., "Constraints on the size of Martian aerosols from Thermal Emission Spectrometer Observations," *J. of Geophysical Research*, Vol. 108, 2003, pp. 1-23.
- [18] Zurek, R.W. and Smrekar, S.E., "An overview of the Mars Reconnaissance Orbiter (MRO) science mission," *J. of Geophys. Res.: Planets*, 112, 2007, pp. 1-22.
- [19] Conrath, B.J., "Thermal structure of the Martian atmosphere during the dissipation of the dust storm of 1971," *Icarus*, Vol. 24, 1975, pp. 36-46.
- [20] Forget, F., Hourdin, F., Fournier, R., Hourdin, C., Talagrand, O., Collins, M., Lewis, S.R., Read, P.L., and Huot, J.-P., "Improved general circulation models of the Martian atmosphere from the surface to above 80 km," *Journal of Geophysical Research*, Vol. 104, 1999, pp. 155-175.

- [21] Murphy, J.R., Pollack, J.B., Haberle, R.M., Leovy, C.B., Toon, O.B., and Schaeffer, J., "Three-dimensional numerical simulation of Martian global dust storms," *J. of Geophys. Research*, Vol. 100, No. E12, 1995, pp. 357-376.
- [22] https://atmos.nmsu.edu/data_and_services/atmospheres_data/MARS/mcs.html
- [23] Bailey, A.B. and Hiatt, J., "Free-Flight Measurements of Sphere Drag at Subsonic, Transonic, Supersonic, and Hypersonic Speeds for Continuum, Transition, and Near-Free-Molecular Flow Conditions," AEDC-TR-70-291, 1971.
- [24] Loth, E., "Compressibility and Rarefaction Effects on Drag of a Spherical Particle," *AIAA Journal*, Vol. 46, No. 9, 2008, pp. 2219-2228.
- [25] Henderson, C.B., "Drag Coefficients of Spheres in Continuum and Rarefield Flows," *AIAA Journal*, Vol. 14, No. 6, 1976, pp. 707-718.
- [26] Ching, E. and Ihme, M., "Sensitivity study of high-speed dusty flows over blunt bodies simulated using a discontinuous Galerkin method," *AIAA Paper* 2019-0895, Jan. 2019.
- [27] Boiko, V.M., Kiselev, V.P., Kiselev, S.P., Papyrin, A.N., Poplavsky, S.V., and Fomin, V.M., "Shock wave interaction with a cloud of particles," *Shock Waves*, Vol. 7, 1997, pp. 275-285.
- [28] Incropera, F.P., DeWitt, D.P., Bergman, T.L., and Lavine, A.S., "Fundamentals of Heat and Mass Transfer, Sixth Edition," John Wiley & Sons, 2007, Chap. 7.
- [29] Drake, R.M., "Forced Convection Heat Transfer from an Isothermal Sphere to Water," *ASME J. of Heat Transfer*, Vol. 32, No. 2, 1961, pp. 170-179.
- [30] Knudsen, J.G. and Katz, D.L., *Fluid Mechanics and Heat Transfer*, McGraw-Hill, New York, NY, 1958.
- [31] Fox, T.W., Rackett, C.W., and Nicholls, J.A., "Shock wave ignition of magnesium powders," *Proceedings of the 11th International Symposium on Shock Tubes and Shock Waves*, University of Washington Press, 1977.
- [32] Kavanau, L.L. and Drake, Jr., R.M., "Heat Transfer from Spheres to a Rarefied Gas in Subsonic Flow," ONR Report He-150-108, 1953.
- [33] Centolanzi, F. and Chapman, D., "Vapor Pressure of Tektite Glass and its Bearing on Tektite Trajectories Determined for Aerodynamic Analysis," *Journal of Geophys. Research*, Vol. 71, No. 6, 1966, pp. 1735-1749.
- [34] Schaefer, L. and Fegley, Jr., B., "A Thermodynamic Model of High Temperature Lava Vaporization on Io," *Icarus*, Vol. 169, 2004, pp. 216-241.
- [35] Scoggins, J.B., "Development of Mutation++: Multicomponent Thermodynamic and Transport Properties for Ionized Plasmas written in C++," *AIAA Paper* 2014-2966, June 2014.
- [36] Haynes, W.M., ed., "CRC Handbook of Chemistry and Physics, 92nd Edition," CRC Press, 2011.
- [37] Melosh, H.J., "A Hydrocode Equation of State for SiO₂," *Meteoritics and Planetary Science*, Vol. 42, No. 12, 2007, pp. 2079-2098.
- [38] Greely, R. and Schultz, P. ed., A Primer in Lunar Geology, Gault, D., "Impact Cratering," NASA TM-62,359, July 1974.
- [39] Flaherty, R.E., "Impact Characteristics in Fused Silica for Various Projectile Velocities," *J. Spacecraft*, Vol. 7, No. 3, 1970, pp. 319-324.
- [40] Cour-Palais, B.G., "Hypervelocity Impact Investigations and Meteoroid Shielding Experience Related to Apollo and Skylab," *Proceedings of the Orbital Debris Workshop*, edited by D. Kessler and S-Y. Su, NASA Conference Publication 2360, 1985.
- [41] Christiansen, E.L. and Ortega, J., "Hypervelocity Impact Testing of Shuttle Orbiter Thermal Protection System Tiles," *AIAA Paper* 90-3666, Sept. 1990.
- [42] Lorenz, G.C., "Simulation of the Erosive Effects of Multiple Particle Impacts in Hypersonic Flow," *Journal of Spacecraft*, Vol. 7, No. 2, 1970, pp. 119-125.
- [43] Keller, K., Lindenmaier, P., Pfeiffer, E.K., Esser, B., Gülhan, A., Marraffa, L., Omary, P., and Desjean, M.C., "Dust Particle Erosion during Mars Entry," *AIAA Paper* 2010-6283, 2010.
- [44] Tran, H., Johnson, C., Rasky, D., Hui, F., Chen, Y.-K., and Hsu, M., "Phenolic Impregnated Carbon Ablators (PICA) for Discovery Class Missions," *AIAA Paper* 96-1911, 1996.
- [45] Schulz, J.C., Stern, E.C., Muppidi, S., and Palmer, G.E., "Development of a Three-Dimensional, Unstructured Material Response Design Tool," *AIAA Paper* 2017-0667, 2017.
- [46] Palmer, G., Schulz, J., and Stern, E., "Material Response Analysis of a Titan Entry Heatshield," *10th Ablation Workshop*, 2018.
- [47] Wright, M. W., White, T., and Mangini, N., "Data Parallel Line Relaxation (DPLR) Code User Manual Acadia – Version 4.01.1," NASA/TM-2009-215388, October 2009.
- [48] Brandis, A.M., White, T.R., Saunders, D.A., Hill, J.P., and Johnston, C.O., "Simulation of the Schiaparelli Entry and Comparison to Aerothermal Flight Data," *AIAA Paper* 2019-3260, June 2019.

- [49] Gülhan, A., Thiele, T., Siebe, F., Kronen, R., and Schleutker, T., “Aerothermal Measurements from the ExoMars Schiaparelli Capsule Entry,” *J. of Spacecraft and Rockets*, Vol. 56, No. 1, 2019, pp. 68-81.
- [50] Johnstone, E., Stindt, T., Merrifield, J., and Ferracina, L., “Analysis of the Aerothermal and Material Performance During the ExoMars Schiaparelli Descent,” *International Conference on Flight Vehicles, Aerothermodynamics, and Re-entry Missions & Engineering (FAR)*, 2019.